Original Article

Characterization and metamorphic evolution of Mesoproterozoic granulites from Sonapahar (Meghalaya), NE India, using EPMA monazite dating

Shyam Bihari Dwivedi (ID), Kevilhoutuo Theunuo and Ravi Ranjan Kumar (ID)

Department of Civil Engineering, Indian Institute of Technology (BHU), Varanasi 221005, India

Abstract

This paper presents three different age domains, obtained by electron microprobe monazite dating, for granulitic gneisses collected from the Shillong-Meghalaya Gneissic Complex in Sonapahar, NE India, which contain radioactive materials, e.g. thorium (3.32–7.20 wt %), uranium (0.133–1.172 wt %) and lead (0.101–0.513 wt %). The microprobe analyses of monazite grains in the rock samples show that the monazites have three different ages ranging from Mesoproterozoic to Neoproterozoic. The oldest age (1571 ± 22 Ma) represents a peak metamorphic event, the youngest dominant age indicates the Pan-African tectonic event (478 ± 7 Ma) and the intermediate age marks the Grenvillian orogeny (1034 ± 91 Ma) or may be a mixing artefact; these ages are located at the cores, rims and intermediate parts of the monazite grains, respectively. The equilibrium mineral phases calculated for the granulitic gneisses from Sonapahar lie in a *P–T* range from 5.9 kbar/754 °C to 8.3 kbar/829 °C in the NCKFMASH system. Plotting the *P–T* conditions of the granulitic gneisses reveals a clockwise *P–T* path. Two major metamorphic events are observed in Sonapahar. The M_1 metamorphic stage is represented by peak mineral assemblages of prograde garnet-forming reactions (8.2 kbar/~713 °C) during Mesoproterozoic time (1571 ± 22 Ma). The M_2 metamorphic stage featured decompression (3.9 kbar/~701 °C) in which garnet–sillimanite broke down to form cordierite along an isothermal decompression path during the Pan-African tectonic event (478 ± 7 Ma).

1. Introduction

The Sonapahar area is situated in the West Khasi Hills district of Meghalaya, NE India, and is a part of the Shillong-Meghalaya Gneissic Complex (SMGC), also known as the Shillong Plateau. The SMGC belongs to the NE portion of India, with the Garo, Khasi and Jaintia hills outlining the southern, northern and western parts of the plateau, respectively. The SMGC is still one of the least-known granulite belts in the world, as little attention has been paid to the basement rocks (Precambrian Litho Units) of northeastern India. This deficiency motivated us to conduct electron microprobe (EPMA) monazite dating of the granulites in the study area to determine the ages of the metamorphic events, i.e., whether they are Palaeoproterozoic or Mesoproterozoic, for correlation of the metamorphic history with global metamorphic events. Different types of amphibolite- to granulite-facies mineral assemblages have been identified in the Sonapahar area of the SMGC, which reflects prograde metamorphism from the greenschist to the granulite facies. A preliminary note on the gneissic complex of the Nongmaweit–Rambrai–Nongstoin Plateau was provided by Ghosh (1952), while Banerjee (1955) noted the petrology of the metamorphites around Sonapahar. Ghosh & Saha (1954) and Lal *et al.* (1978) reported sapphirine-bearing granulites from Sonapahar. The exposure of the basement rocks in the SMGC is limited; thus, granulite-facies rocks are reported only from some parts of the plateau, namely, the Sonapahar area (Lal *et al.* 1978; Chatterjee *et al.* 2007; Dwivedi, 2011; Dwivedi & Theunuo, 2013, 2017), Goalpara Hills (Chatterjee *et al.* 2007, 2011) and Patharkhang (Dwivedi & Theunuo, 2011).

Monazite dating with an electron microprobe has been performed based on the total abundances of Th, U and Pb (Suzuki & Adachi, 1991, 1994; Montel *et al.* 1996; Braun *et al.* 1998; Williams *et al.* 1999, 2007; Suzuki & Kato, 2008; Hazarika *et al.* 2017). The EPMA monazite dating technique can identify the preserved history of polyphase metamorphic events for the comparison of the metamorphic evolution with past geological records. Different methodologies are applied to extract the history of the rock, which provide crucial datasets constraining the evolution of the SMGC. The evolutionary records of granulites are preserved in the form of different mineral assemblages and associations in different rock types, fabrics and textural relationships. The EPMA monazite dating of the metapelitic granulites of the SMGC reveals
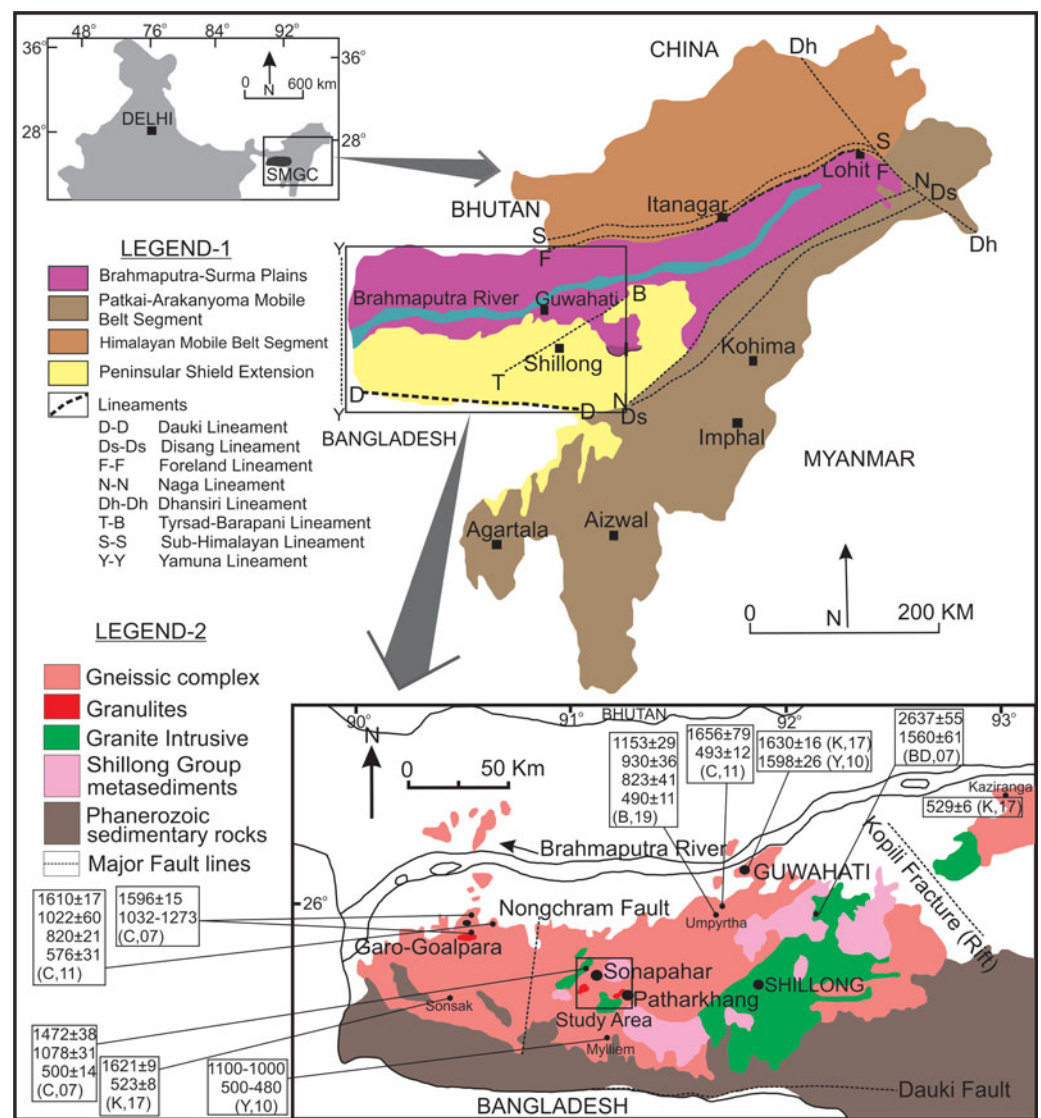
Fig. 1. (Colour online) (a) Inset map showing the location of the Shillong-Meghalaya Gneissic Complex (SMGC) in India. (b) Map showing the different segments and tectonic lineaments of NE India (Sengupta & Agarwal, 1998, modified after Anon, 1974). Rectangle represents the SMGC located in the western part of NE India. (c) Regional geological map of the SMGC (after Mazumdar, 1976). The geochronological dates for the SMGC are from: BD,07 – Bidyananda & Deomurari (2007); C,07 – Chatterjee *et al.* (2007); Y,10 – Yin *et al.* (2010); C,11 – Chatterjee *et al.* (2011); K,17 – Kumar *et al.* (2017); B,19 – Borah *et al.* (2019).

predominantly Mesoproterozoic ages of 1621–1596 Ma for a post-S_1/pre-S_2 stage of metamorphism, with poorly constrained 1141–946 Ma ages and more significant ages of 649–524 Ma, which are considered syn-S_2 and post-S_2 stages of metamorphism, respectively (Chatterjee *et al.* 2007, 2011; Chatterjee, 2017). U–Pb zircon dating of granite gneiss basement rocks from the central SMGC yielded Neoarchaean to Neoproterozoic ages, which range from ~2600 to ~1100 Ma (Bidyananda & Deomurari, 2007; Kumar *et al.* 2017). Yin *et al.* (2010) found three stages of granite intrusion at ~1.6 Ga, ~1.1 Ga and ~0.5 Ga in the central SMGC, which were revealed by the same analytical technique. In the present study, an attempt has been made to meticulously study the granulites of Sonapahar based on the most recent methodology (monazite dating, bulk composition modelling and *P–T* conditions) employed for the interpretation of its metamorphic evolution and correlation with global tectonics.

2. Geological setting

The SMGC is located in the northeastern extension of the Indian Peninsular Precambrian shield, and comprises the NE–SW-trending Proterozoic Shillong basin with metasedimentary rocks of the

Shillong Group (Bidyananda & Deomurari, 2007; Yin *et al.* 2010) (Fig. 1). The area around Sonapahar (latitude 25° 39′ N to 25° 42′ N and longitude 91° 01′ E to 91° 07′ E) is located along the eastern part of the Nongchram fault (Gupta & Sen, 1988; Golani, 1991) (Fig. 1). This area lies in the central part of the SMGC and is ~60 km west of the town of Shillong (Fig. 2).

The SMGC is surrounded in the north by the Oldham and Brahmaputra Valley faults and in the south by the N-dipping Dauki fault and its related fold system, while the western portion of the plateau is bounded by the N–S Jamuna fault; along the eastern side, it is bordered by the Indo-Myanmar mobile belt and Kopili rift, which separate the plateau from the Mikir Hills (Evans, 1964; Desikachar, 1974; Acharyya *et al.* 1986; Nandy, 1986, 2001; Gupta & Sen, 1988; Rajendran *et al.* 2004; Yin *et al.* 2010) (Fig. 1). The SMGC is separated from the main Indian Peninsular shield by the Cretaceous Rajmahal volcanic rocks and Tertiary Ganges–Brahmaputra alluvium; the plateau covers an area of ~47000 km^2 (Fig. 1). Desikachar (1974) proposed that the SMGC is part of the eastern extension of the Chhotanagpur gneissic complex (CGC) and the Central Indian Tectonic Zone (CITZ) of central India. The ENE–WSW-trending CITZ was formed by the collision and suturing of the North Indian Block
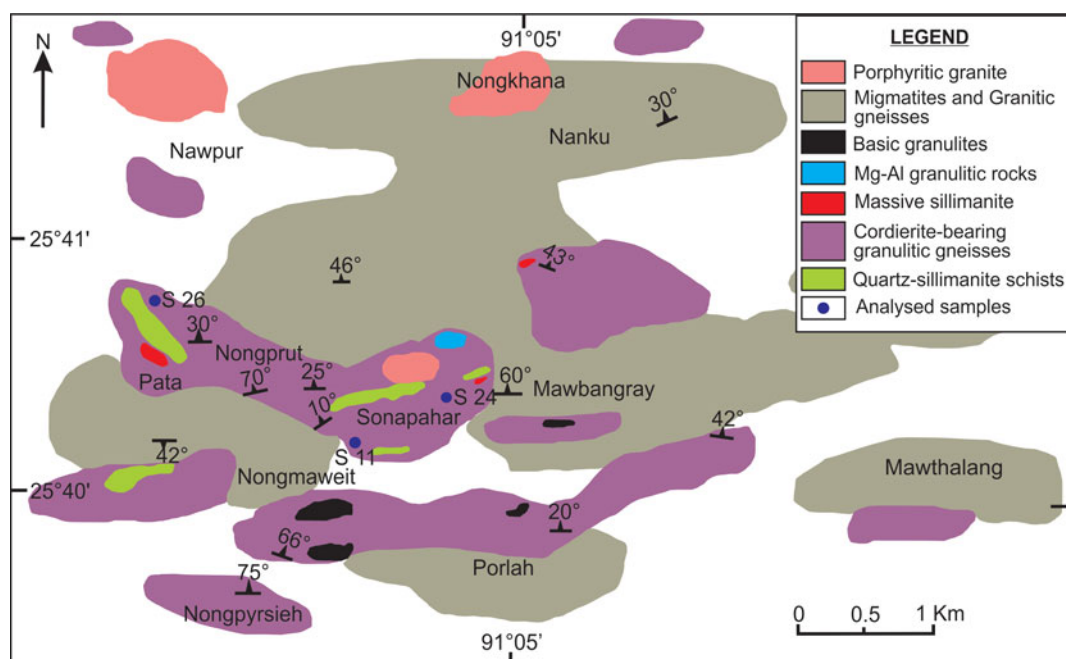
Fig. 2. (Colour online) Geological map of Sonapahar (rectangular area in Fig. 1c) showing different rock types present in the study area.

(NIB) and South Indian Block (SIB) at ∼1.5 Ga due to the subduction of the SIB under the NIB in the Indian Peninsular shield (Bhowmik *et al.* 2012, 2014). Some authors have also suggested that the NIB was subducted southward below the SIB (Yedekar *et al.* 1990; Mishra *et al.* 2000), and another proposal was double-sided subduction (Naganjaneyulu & Santosh, 2010). However, the northeastern part of the Indian Plate is subducting under the Tibetan Plateau from the north; in the same way, the Burmese Plate is also over-riding it from the east. Thus, the Shillong Plateau is a mobile foreland spur, which tends to resist the Burmese block that is moving westward (Desikachar, 1974).

The Proterozoic metasedimentary rocks and the basement gneisses are composed of amphibolite- to granulite-facies rocks derived from Neoarchaean–Palaeoproterozoic gneissic rocks (Chatterjee, 2017 and references therein). The Sonapahar area is composed of granulite-facies metapelites and quartzofeldspathic gneisses, including sillimanite-bearing gneisses, basic granulites, amphibolites and granite gneisses (Lal *et al.* 1978; Nandy, 2001; Dwivedi & Theunuo, 2013, 2017). However, the Sonapahar area has a significant occurrence of metapelitic granulites and has experienced multiple phases of deformation (Chatterjee *et al.* 2007; Chatterjee, 2017). There are three stages of metamorphism occurring in the metapelites, and they were metamorphosed along a counter-clockwise *P–T* path (Chatterjee *et al.* 2007).

The SMGC was assembled with the Columbia, Rodinia and Gondwana supercontinents during different periods of tectonic orogeny. Rodinia was an accretionary product of fragmented plates from the Columbia supercontinent, with rifting starting in Mesoproterozoic times (∼1.5 Ga). Three episodes of magmatism (∼ 1.5, ∼ 1.0 and ∼ 0.5 Ga) were reported from the SMGC based on U–Pb zircon dating (Yin *et al.* 2010), which are consistent with the metamorphic events demarcated by monazite dating (Chatterjee *et al.* 2007). This correlation suggests that the magmatism and metamorphic events were related to each other. A chemical age of 1.15–0.93 Ga reveals the SMGC was situated adjacent to East Antarctica (Prydz Bay) during the Rodinia amalgamation

(Borah *et al.* 2019). The SMGC was located to the north of the NW-trending Eastern Ghats orogeny, and it was considered a part of the Rodinia supercontinent (∼1.0 Ga), which was produced by India–Antarctica collision (Dalziel, 1991; Hoffman, 1991; Moores, 1991; Li *et al.* 2008). The high-grade rocks of the Eastern Ghats Mobile Belt of the Indian Plate correlated with the Napier and Rayner Province in East Antarctica during the Grenvillian orogeny (∼1.0 Ga) (Mezger & Cosca, 1999; Boger *et al.* 2000; Fitzsimons, 2000). The Rodinia supercontinent achieved the highest strength of accretion during the Grenvillian orogeny (∼1.0 Ga), after which drifting was again started from ∼0.75 Ga, finally forming the Gondwana supercontinent during Neoproterozoic times (∼0.5 Ga) (Rogers & Santosh, 2002; Chatterjee *et al.* 2007, 2011; Li *et al.* 2008; Yin *et al.* 2010; Kumar *et al.* 2017; Borah *et al.* 2019). This orogeny experienced significant magmatism and contraction during the amalgamation of Eastern Gondwana (0.55–0.50 Ga) (Ghosh *et al.* 2004; Collins *et al.* 2007; Biswal *et al.* 2007). Several authors have suggested that the western margin of the Pan-African suture passing through Prydz Bay in Antarctica possibly passes through the SMGC (Fitzsimons, 2000, 2003; Chatterjee *et al.* 2007; Kelsey *et al.* 2008). The SMGC and Prydz Bay belt witnessed their latest high-grade event and have a shared common Early Palaeozoic metamorphic history during the final stages of metamorphism related to the Pan-African collision (∼0.5 Ga). The Prydz Bay Pan-African suture continues through the SMGC in NE India (Chatterjee *et al.* 2011). According to Gupta & Sen (1988), the SMGC lies along the direct continuation of the Ninety-East Ridge. They also considered that a major N–S-trending lineament called the Um-Ngot lineament that developed during Late Jurassic to Early Cretaceous times might constitute a location for neotectonic activity in the SMGC (Srivastava *et al.* 2019 and references therein). Additionally, the oblique northeastward counter-clockwise movement of the Indian Plate has produced severe compressional tectonics; hence, the SMGC is tectonically sensitive and seismically very active (Harijan *et al.* 2003; Ramesh *et al.* 2005).

3. Sample collection, preparation and analytical techniques

Geological mapping and the collection of 40 representative rock samples from the Sonapahar area were carried out during different courses of fieldwork. Representative samples of all available rock outcrops were collected. A Global Positioning System instrument (Garmin GPSMAP 78s) was used to record the locations (latitude/longitude) of the collected samples, and these data are presented in online Supplementary Material Table S1.

Thin-sections of all collected rock samples were prepared, and, after fine polishing, the slides were studied under a Leica petrological microscope (LEICA DM 2500 P). The detailed petrographic study revealed different types of mineral assemblages and textures. Based on the petrography, thin-sections of different important rocks were selected for further probe analysis.

We chose three samples (Sn-26, Sn-24 and Sn-11) for the electron microprobe analyses, which were carried out at the Geological Survey of India (GSI) laboratory in Faridabad, and IIT Kharagpur (CAMECA SX100 EPMA). The minerals were analysed with a CAMECA SX100 electron microprobe in Faridabad. Different accelerating voltages and standards were used for silicate analysis and monazite mineral dating. The polished thin-section was coated with a 40 nm layer of carbon for electron microprobe analysis using a LEICA-EM ACE200 carbon coating instrument. For silicate analysis, the accelerating voltage was 15 kV with a beam current of 10 nA and a beam diameter of 1 micron. Andradite was used as a natural silicate mineral to verify crystal positions using an internal standard (SP2-LiF, SP3-LPET, SP4-LTAP and SP5-PET) with wavelength dispersive (WD) spectrometers (SP#) in the CAMECA SX100 instrument. The standards used for different elements were Al (Al_2O_3), Si and Ca ($CaSiO_3$), Ti (TiO_2), Cr (Cr), Zn (Zn), Na (albite), K (orthoclase), Fe (Fe_2O_3), Mn (rhodonite), Mg (peridotite), Ba ($BaSO_4$), F (CaF_2), Na (NaCl) and P (apatite); a Ni pure metal standard was supplied by CAMECA-AMETEK, which was used for routine calibration and quantification. For monazite, the accelerating voltage was 20 kV with a beam current of 200 nA and a beam diameter of 2 microns. The counting times were 240 s (U and Pb), 120 s (Th and Y), 30 s (Pr, Sm, Gd and Dy), 20 s (La, Ce and Nd) and 10 s (Si, P and Ca); U was measured using U Mβ X-ray intensity with corrections performed for Th Mc interference. Interference correction was also performed for Th Mz and Y Lc3 overlap on Pb Mα X-ray intensity. Other X-ray lines were used for different elements: Kα (Si, P and Ca), Lα (Y, La and Ce), Lβ (Pr, Nd, Sm and Dy) and Mα (Th). Quantification of rare earth element (REE) analyses in monazite mineral phases and U, Th and Y elemental X-ray mapping of monazite grains were obtained at an accelerating voltage of 20 kV, with a beam current of 200 nA and 0.5 μm/pixel spatial resolution. All REE analyses were carried out on LiF crystals attached to SP2, and Pb, Th and U were analysed with LPET crystals connected with the SP3 spectrometer in a CAMECA-SX100 EPMA instrument. Synthetic glass standards of all REEs (La to U) supplied by CAMECA-AMETEK were used for routine calibration and quantification.

4. Rock types and their field relationships

4.a. Mineral assemblages and textural relationship

The investigated area contains different types of rocks: granulitic gneisses, migmatites, cordierite–sillimanite gneisses, Mg–Al granulitic rocks, biotite gneisses, quartz–sillimanite schists, two-pyroxene-bearing basic granulites, massive sillimanite rocks

and coarse-grained porphyritic granites (Fig. 2). The garnet–cordierite-bearing granulitic gneiss (Sn-26), garnet-absent cordierite-bearing granulitic gneiss (Sn-24) and cordierite–spinel-bearing granulitic gneiss (Sn-11) were studied in detail for the purpose of monazite dating. The mineral abbreviations used in this study are from Whitney & Evans (2010).

4.a.1. Garnet–cordierite-bearing granulitic gneiss

The garnet–cordierite-bearing granulitic gneiss (Sn-3, Sn-26 and Sn-27a, b) is massive and dark grey, mostly medium grained, and shows a granulitic texture. In sample Sn-26, porphyroblasts of quartz and cordierite can be clearly observed (Fig. 3a) with a pitted appearance, which is probably due to pinitization of the cordierite grains. Microscopically, these rocks contain garnet, cordierite, biotite, quartz, plagioclase, K-feldspar (mostly perthitic) and sillimanite. In addition, the accessory minerals present in minor amounts are magnetite, ilmenite, rutile, zircon, monazite, etc. Garnet occurs as medium- to large-sized, subhedral and rounded grains within the groundmass. Fine to medium flakes of biotite grains are found wrapping the boundaries of garnet and cordierite, whereas biotite and sillimanite occur as inclusions in garnet (Fig. 3b).

4.a.2. Garnet-absent cordierite-bearing granulitic gneiss

Different representative samples (Sn-4a,b, Sn-5a,b,c, Sn-7, Sn-21, Sn-22, Sn-23 Sn-24a,b,c and Sn-25) of garnet-absent cordierite-bearing granulitic gneiss were collected from the study area. These rocks consist of cordierite, biotite, plagioclase, sillimanite, K-feldspar and quartz with minor amounts of the accessory minerals ilmenite, magnetite, zircon, rutile, monazite, etc. Cordierite grains occur as medium to coarse anhedral phenocrysts, whereas biotite, sillimanite and quartz occur as inclusions (Fig. 3c). Biotite grains occur mostly as small flakes in the groundmass, defining the foliation.

4.a.3. Cordierite–spinel-bearing granulitic gneiss

Samples Sn-9a,b, Sn-10 and Sn-11a,b include cordierite, spinel, biotite, sillimanite, K-feldspar, quartz and magnetite. They also contain minerals such as ilmenite, monazite and zircon as accessory phases. Cordierite occurs as medium- to coarse-grained poikiloblasts that contain numerous inclusions of spinel, sillimanite and magnetite as possible prograde minerals (Fig. 3h).

4.b. Petrography and mineral chemistry

4.b.1. Garnet

Garnet crystals in Sn-26 are characterized by their isotropic optical properties and range in diameter from 0.1 to 0.6 mm. Two generations of garnets occur in the garnet–cordierite-bearing granulitic gneisses, out of which the prograde garnets contain inclusions of biotite and trails of sillimanite needles (Fig. 3b). The textural relationships of the garnets suggest that crystallization of the garnets is related to the prograde metamorphic event via metamorphic reaction 1.

The prograde garnet coexists with biotite–sillimanite–K-feldspar–plagioclase–quartz with other minor phases of rutile and ilmenite. The second stage of garnet participates in a retrograde decompression reaction and coexists with garnet–cordierite–sillimanite–quartz and garnet–cordierite–sillimanite–biotite–K-feldpar–plagioclase–quartz. The electron microprobe compositional mapping of the garnets across the crystals shows that the garnets from Sonapahar are rich in Fe and Mn and poor in Ca and Mg.
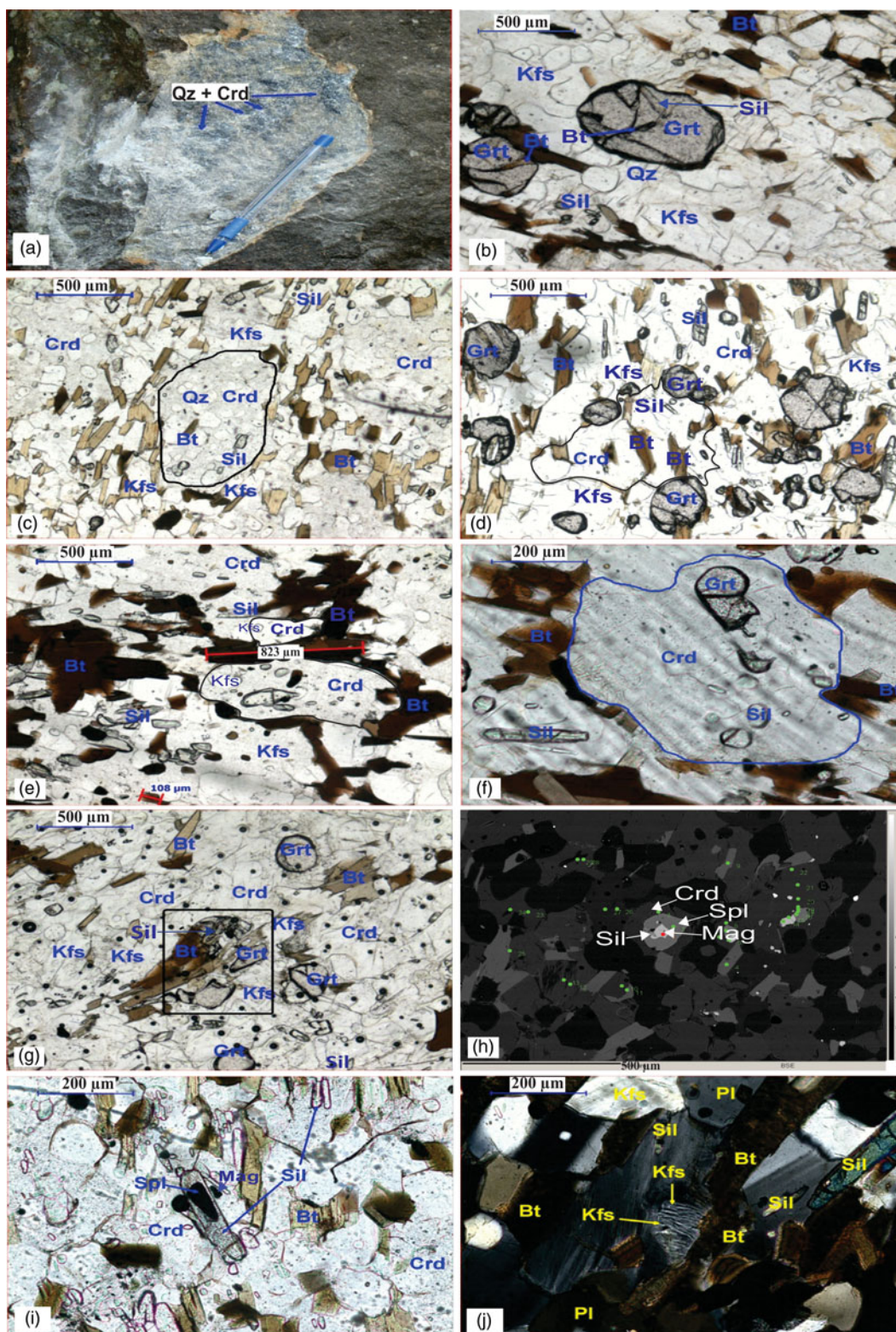
Fig. 3. (Colour online) (a) Field photograph showing porphyroblasts of quartz and cordierite in garnet–cordierite-bearing granulitic gneisses. (b) Photomicrograph of coarse xenoblasts of garnet sillimanite in granulitic gneiss showing dodecahedral outline and inclusions of trails of biotite (plain-polarized light; PPL). (c) Photomicrograph of large poikiloblasts of cordierite with trails of sillimanite and biotite occurring as inclusions (PPL). (d) Photomicrograph showing small grains of sillimanite and biotite occurring as inclusions within cordierite, and garnet coexisting with cordierite in cordierite-bearing granulitic gneiss (PPL). (e) Photomicrograph showing biotite flakes wrapped around cordierite grains and aligned to S_2 foliation; some flakes also define S_3. The intergrowth of biotite and sillimanite is also observed (PPL). (f) Photomicrograph showing poikiloblasts of cordierite with sillimanite and garnet occurring as inclusions (PPL). (g) Photomicrograph showing corroded porphyroblast of garnet is breaking down to biotite and cordierite (PPL). (h) Back-scattered electron (BSE) image of corona texture in which magnetite at the core is rimmed by spinel followed by cordierite. (i) Photomicrograph of corona texture in which dark green spinel is rimmed by sillimanite, which occurs within the poikiloblastic cordierite (PPL). (j) Hair perthite intergrowth of plagioclase and K-feldspar showing quadrille structure in granulitic gneiss (cross-polarized light; XPL) (mineral abbreviations from Whitney & Evans, 2010).

Table 1. Representative electron microprobe analysis of garnet from Sonapahar granulitic gneisses

Sample No.	Sn-26/1c	Sn-26/1r	Sn-26/2c	Sn-26/9	Sn-26/22
Oxide wt %					
SiO_2	37.43	37.56	37.26	37.47	38.01
TiO_2	0.05	0.05	0.07	0.03	0.01
Al_2O_3	20.89	20.94	21.12	21.23	20.94
Cr_2O_3	0.10	0.00	0.02	0.09	0.07
FeO	34.37	34.11	33.32	33.49	34.15
MnO	3.48	3.58	3.59	3.29	3.77
MgO	2.85	2.66	2.98	2.94	2.56
CaO	0.86	0.64	0.68	0.64	0.68
Total	100.03	99.54	99.04	99.18	100.19
Cations for 12 oxygen atoms					
Si	3.02	3.04	3.03	3.03	3.03
ΣZ	3.02	3.04	3.03	3.03	3.03
Al^{VI}	1.99	1.98	1.99	1.99	1.98
Ti	0.003	0.003	0.004	0.002	0.000
Cr	0.007	0.000	0.001	0.006	0.005
ΣY	2.000	1.983	1.995	1.998	1.985
Fe	2.32	2.31	2.28	2.29	2.33
Mn	0.24	0.25	0.25	0.23	0.26
Mg	0.34	0.33	0.36	0.36	0.31
Ca	0.075	0.056	0.06	0.056	0.06
ΣX	2.975	2.936	2.96	2.936	2.96
Almandine	77.96	78.69	77.26	78.08	78.64
Pyrope	11.51	11.00	12.28	12.24	10.53
Grossularite	2.52	1.91	2.03	1.91	2.02
Spessartine	8.01	8.41	8.43	7.77	8.81
X_{Mg}	0.13	0.12	0.14	0.14	0.12

Where, $X_{Mg} = Mg/(Fe + Mg)$; r – rim; c – core

The garnets consist of 77.26 to 78.69 mol. % almandine, 10.53 to 12.28 mol. % pyrope, 1.91 to 2.52 mol. % grossularite and 7.77 to 8.81 mol. % spessartine (Table 1).

4.b.2. Sillimanite

Sillimanite occurs as needles or fibrolites (0.07 to 0.5 mm in length) intimately intergrown with biotite. Most of the sillimanite needles and biotite flakes occur as inclusions within the porphyroblasts of cordierite, whereas garnet porphyroblasts occur within the matrix or adjacent to the cordierite (Fig. 3d), which suggests prograde metamorphic reaction 3.

4.b.3. Biotite

Biotite is pleochroic with brown or yellowish brown to reddish or dark brown colours, and biotite flakes range from 0.1 to 0.8 mm in length. The parallel orientation of biotite flakes and intergrowths of biotite and sillimanite are also observed, which are wrapped around the cordierite grains and aligned to the S_2 foliation, with

Table 2. Representative electron microprobe analysis of biotite from Sonapahar granulitic gneisses

Sample No.	Sn-11/2c	Sn-11/3r	Sn-26/2r	Sn-26/3c	Sn-26/2c
Oxide wt %					
SiO_2	34.70	34.90	34.40	35.00	34.80
TiO_2	3.42	3.79	3.08	3.49	3.72
Al_2O_3	17.20	16.60	16.70	17.80	17.50
Cr_2O_3	0.00	0.00	0.13	0.00	0.07
FeO	21.40	20.00	21.70	21.70	21.20
MnO	0.18	0.07	0.08	0.11	0.05
MgO	8.32	8.71	7.86	7.19	7.28
CaO	0.00	0.00	0.29	0.03	0.01
Na_2O	0.14	0.14	0.09	0.18	0.10
K_2O	9.70	9.73	9.40	9.34	9.44
Cl	0.04	0.03	0.01	0.02	0.03
F	1.23	1.33	1.46	0.96	1.21
Total	96.33	95.30	95.20	95.82	95.41
Cations for 11 oxygen atoms					
Si	2.72	2.72	2.70	2.71	2.73
Al^{IV}	1.28	1.28	1.3	1.29	1.27
ΣZ	4	4	4	4	4
Al^{VI}	0.30	0.25	0.26	0.33	0.32
Ti	0.20	0.22	0.18	0.20	0.18
Cr	0.00	0.00	0.01	0.00	0.01
Fe^{2+}	1.40	1.31	1.44	1.41	1.41
Mn	0.01	0.01	0.01	0.01	0.00
Mg	0.97	1.01	0.93	0.83	0.87
ΣY	2.88	2.80	2.83	2.78	2.79
Ca	0.00	0.00	0.03	0.00	0.00
Na	0.02	0.02	0.01	0.03	0.02
K	0.97	0.97	0.98	0.96	1.00
ΣX	0.99	0.99	1.02	0.99	1.02
Cl	0.01	0.01	0.01	0.01	0.01
F	0.31	0.33	0.35	0.24	0.30
X_{Mg}	0.43	0.44	0.39	0.37	0.38

Where, $X_{Mg} = Mg/(Fe + Mg)$; r – rim; c – core

some flakes defining S_3 (Fig. 3e). This textural condition suggests retrograde reaction 4.

The X_{Mg} of the biotite is low and ranges from 0.37 to 0.44. The TiO_2 in the biotites from the samples of the granulitic gneisses ranges from 3.08 to 3.79 wt % (Table 2).

4.b.4. Cordierite

Cordierite is characterized by yellow pleochroic haloes with polysynthetic and sector twinning. Cordierite mainly occurs as coarse porphyroblasts (sizes 0.8 to 1.5 mm) and contains inclusions of biotite and sillimanite (Fig. 3c) suggesting reaction 2.

Table 3. Representative electron microprobe analysis of cordierite from Sonapahar granulitic gneisses

Sample No.	Sn-26/3c	Sn-26/6r	Sn-11/9	Sn-11/10	Sn-11/11
Oxide wt %					
SiO_2	48.74	48.93	48.78	48.54	49.19
TiO_2	0.02	0.04	0.02	0.00	0.00
Al_2O_3	32.44	32.48	32.49	32.71	32.91
Cr_2O_3	0.02	0.12	0.06	0.00	0.00
FeO	8.53	8.77	8.31	8.74	8.19
MnO	0.19	0.21	0.26	0.34	0.27
MgO	8.06	8.02	8.31	8.24	8.14
Na_2O	0.04	0.06	0.03	0.11	0.13
Total	98.04	98.63	98.26	98.68	98.83
Cations for 18 oxygen atoms					
Si	5.03	5.03	5.02	4.99	5.03
Al^{IV}	3.95	3.94	3.94	3.95	3.97
ΣZ	8.98	8.97	8.96	8.94	9.00
Ti	0.002	0.003	0.001	0.00	0.00
Cr	0.002	0.01	0.005	0.00	0.00
Fe^{2+}	0.74	0.75	0.72	0.75	0.70
Mn	0.02	0.02	0.02	0.03	0.02
Mg	1.24	1.23	1.27	1.24	1.24
ΣY	1.994	2.013	2.016	2.02	1.96
Na	0.008	0.012	0.006	0.019	0.026
ΣX	0.008	0.012	0.006	0.019	0.026
X_{Mg}	0.63	0.62	0.64	0.62	0.64

Where, $X_{Mg} = Mg /(Fe + Mg)$; r – rim; c – core

Table 4. Representative electron microprobe analysis of spinel from Sonapahar granulitic gneisses

Sample No.	Sn-11/1c	Sn-11/1r	Sn-11/16	Sn-11/17
Oxide wt %				
SiO_2	0.11	0.03	0.71	0.21
TiO_2	0.01	0.02	0.04	0.06
Al_2O_3	56.10	55.80	56.60	55.80
Cr_2O_3	0.76	1.12	1.23	1.21
Fe_2O_3	2.98	2.86	1.20	1.62
FeO	36.30	35.70	35.10	35.90
MnO	0.36	0.34	0.46	0.27
MgO	4.01	3.98	3.87	4.23
CaO	0.00	0.00	0.05	0.01
Na_2O	0.02	0.05	0.04	0.03
Total	100.65	99.9	99.3	99.34
Cations for 4 oxygen atoms				
Si	0.01	0.00	0.03	0.01
Ti	0.00	0.00	0.00	0.00
Al	1.95	1.94	1.96	1.94
Cr	0.01	0.03	0.03	0.03
ΣZ	1.97	1.97	2.02	1.98
Fe^{3+}	0.06	0.06	0.03	0.04
Fe^{2+}	0.91	0.88	0.87	0.89
Mn	0.01	0.01	0.01	0.01
Mg	0.16	0.15	0.15	0.17
Ca	0.00	0.00	0.00	0.00
Na	0.00	0.00	0.00	0.00
ΣY	1.14	1.10	1.06	1.11
X_{Mg}	0.14	0.14	0.14	0.16

Where, $X_{Mg} = Mg/(Fe + Mg)$; r – rim; c – core

Cordierite also contains xenoblastic to sub-idioblastic garnets, rounded blebs of quartz and sillimanite as inclusions (Fig. 3f). This textural relationship suggests metamorphic reaction 5. Highly corroded garnet also occurs within the cordierite porphyroblasts with adjacent large biotite flakes (Fig. 3g). The textural relationships of the garnet suggest decompression reaction 6.

The cordierite analyses show summations of between 98.04 and 98.83 wt %, suggesting that this mineral may be hydrous, containing 1.17–1.96 wt % H_2O and gaseous species. The X_{Mg} ranges between 0.62 and 0.64 (Table 3).

4.b.5. Spinel

Spinel from Sn-11 appears in garnet-absent cordierite-bearing granulitic gneisses and shows granular exsolution of magnetite. A corona texture forms in which magnetite at the core is rimmed by spinel followed by cordierite porphyroblasts (Fig. 3h) and suggests prograde reaction 7 for the appearance of spinel.

Sharp grain contacts between spinel and sillimanite are observed. Spinel also occurs as inclusions within sillimanite (Fig. 3i). At times, both sillimanite and spinel occur as inclusions within cordierite porphyroblasts, suggesting reaction 8.

The X_{Mg} of spinel in the granulitic gneiss ranges from 0.14 to 0.16 (Table 4). This wide range of X_{Mg} suggests a solid solution from spinel ($MgAl_2O_4$) to hercynite ($Fe^{2+}Al_2O_4$).

4.b.6. Feldspar

K-feldspar is mostly mesoperthitic with lamellar intergrowths of plagioclase in the main masses of K-feldspar characterized by a quadrille structure (Fig. 3j). These grains also form a mosaic fabric with garnet, biotite and quartz. At times, contacts between K-feldspar and biotite are serrated. Myrmekitic intergrowths with vermicules of quartz and clear albite with characteristic lamellar twinning occur between K-feldspar grains and K-feldspar–plagioclase grains. The $X_{Ca} = Ca/(Na + Ca + K)$ ratio of the granulitic gneisses ranges from 0.01 to 0.31 (Table 5). A minor component of Fe is observed in the plagioclase, which is present as Fe^{3+} (0.00 to 0.02 pfu). This component may be due to Al^{3+} substitution or to extremely fine inclusions of opaque minerals in the plagioclase.

The metamorphic reactions 1 to 8 discussed in Sections 4.b.1 to 4.b.5, on the basis of the textural relationships of the coexisting mineral phases, are presented in Section 5 below.

5. Metamorphic evolution

The metamorphic evolution of the granulites from the area around Sonapahar (Riangdo) has been documented based on detailed

Table 5. Representative electron microprobe analysis of plagioclase and K-feldspar from Sonapahar granulitic gneisses

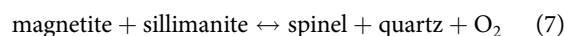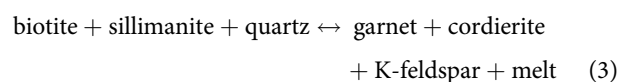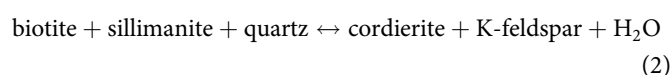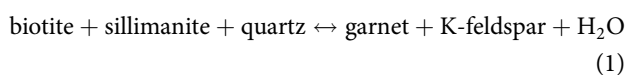| Sample No.	Sn-11/13	Sn-11/27r	Sn-26/1c	Sn-26/1r	Sn-26/7
Oxide wt %					
SiO_2	68.10	60.48	63.05	63.00	62.12
TiO_2	0.03	0.00	0.01	0.04	0.07
Al_2O_3	19.40	24.56	24.8	23.77	23.35
Fe_2O_3	0.00	0.00	0.47	0.11	0.38
MnO	0.00	0.03	0.04	0.06	0.08
MgO	0.01	0.00	0.13	0.01	0.12
CaO	0.22	6.37	3.69	4.02	4.97
Na_2O	10.81	7.88	8.65	9.10	8.45
K_2O	1.62	0.13	0.14	0.11	0.07
Total	100.25	99.45	100.97	100.22	99.6
Cations for 8 oxygen atoms					
Si	2.99	2.70	2.75	2.76	2.76
Ti	0.00	0.00	0.00	0.00	0.01
Al	1.00	1.29	1.28	1.23	1.23
Fe^{3+}	0.00	0.00	0.02	0.01	0.01
Mn	0.00	0.00	0.00	0.01	0.01
Mg	0.00	0.00	0.01	0.00	0.01
$\sum Z$	4.00	3.99	4.06	4.01	4.03
Ca	0.01	0.31	0.17	0.24	0.24
Na	0.92	0.68	0.73	0.77	0.73
K	0.09	0.01	0.01	0.01	0.01
$\sum X$	1.02	1.00	0.91	1.02	0.98
X_{Ca}	0.01	0.31	0.19	0.23	0.24

Where, $X_{Ca} = Ca/(Ca + Na + K)$, r – rim, c – core

petrological studies, reaction textures, monazite dating, bulk composition modelling and the *P–T* path of metamorphism.
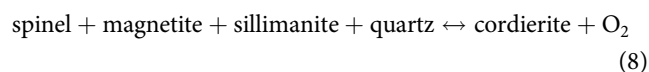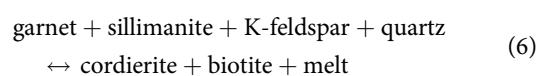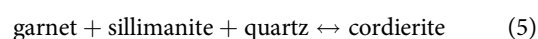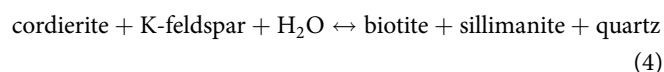
5.a. Metamorphic stages and deformation

Detailed petrographic studies on the different types of rocks reveal several diverse mineral assemblages in Sonapahar that exhibit various mineral reaction textures. These textural relationships suggest different mineral reactions, which are discussed in Sections 4.b.1 to 4.b.5.

In the granulitic gneiss, the textural relationships of the garnet suggest two phases of crystallization in which the first prograde garnet formed due to the breakdown of biotite and is related to the first metamorphic event (M_1). The following prograde and retrograde/decompression reactions are referred to the M_1 and M_2 metamorphic events, respectively.

(a) Prograde reactions during M_1

$$\text{biotite} + \text{sillimanite} + \text{quartz} \leftrightarrow \text{garnet} + \text{K-feldspar} + H_2O \tag{1}$$

$$\text{biotite} + \text{sillimanite} + \text{quartz} \leftrightarrow \text{cordierite} + \text{K-feldspar} + H_2O \tag{2}$$

$$\text{biotite} + \text{sillimanite} + \text{quartz} \leftrightarrow \text{garnet} + \text{cordierite} + \text{K-feldspar} + \text{melt} \tag{3}$$

$$\text{magnetite} + \text{sillimanite} \leftrightarrow \text{spinel} + \text{quartz} + O_2 \tag{7}$$

(b) Retrograde/decompression reactions during M_2

$$\text{cordierite} + \text{K-feldspar} + H_2O \leftrightarrow \text{biotite} + \text{sillimanite} + \text{quartz} \tag{4}$$

$$\text{garnet} + \text{sillimanite} + \text{quartz} \leftrightarrow \text{cordierite} \tag{5}$$

$$\text{garnet} + \text{sillimanite} + \text{K-feldspar} + \text{quartz} \leftrightarrow \text{cordierite} + \text{biotite} + \text{melt} \tag{6}$$

$$\text{spinel} + \text{magnetite} + \text{sillimanite} + \text{quartz} \leftrightarrow \text{cordierite} + O_2 \tag{8}$$

Here, reaction 1 is responsible for the formation of prograde garnet in the absence of cordierite, whereas reactions 3, 5 and 6 appear in the garnet–cordierite-bearing granulitic gneiss, and reactions 2 and 4 are observed in the garnet-absent cordierite-bearing granulitic gneiss; however, reactions 7 and 8 are involved in the cordierite–spinel-bearing granulitic gneiss.

5.b. P–T pseudosection

Based on the mineral assemblages observed for the granulitic gneisses (Sn-3, Sn-26 and Sn-27a, b), a *P–T* pseudosection for mineral equilibria modelling was calculated using THERMOCALC v.3.33 (Powell & Holland, 1988, updated June 2009). For the granulitic gneiss, the calculations were carried out in the NCKFMASH model system. The average chemical composition (in mol %) of the granulitic gneiss is $SiO_2 = 67.74$, $Al_2O_3 = 10.75$, $FeO = 5.36$, $MgO = 6.37$, $CaO = 0.78$, $Na_2O = 1.39$, $K_2O = 2.26$ and $H_2O = 5.35$. The MnO content is very low (0.07 wt %) in these samples, so it is neglected in the modelling. Different mixing models of minerals are used for the calculation of the pseudosection. The NCKFMASH system utilizes garnet, biotite and liquid (melt) from White *et al.* (2007), cordierite from Holland & Powell (1998), and alkali-feldspar and plagioclase from Holland & Powell (2003). The NCKFMASH pseudosection consists of the minerals garnet, cordierite, biotite, K-feldspar and sillimanite, whereas quartz, liquid and plagioclase are taken as saturate phases.

The *P–T* pseudosection in the NCKFMASH model system is calculated for the specific bulk composition of the Sonapahar granulitic gneisses. The NCKFMASH system is calculated with the addition of Na_2O and the appearance of one mineral phase (plagioclase) (White *et al.* 2001), by which we obtain one di-variant, five tri-variant and five tetra-variant fields in a *P–T* range from 2 to 10 kbar and 650 to 900 °C (Fig. 8). The stable mineral equilibria are calculated for the NCKFMASH system with the peak assemblage (garnet–biotite–sillimanite–K-feldspar–plagioclase–liquid–quartz) stable in the *P–T* range of 6.7 kbar/774 °C to 8.3 kbar/829 °C, and it also participates in the appearance of

Table 6. Representative mineral chemistry data of monazite from Sonapahar granulitic gneisses

Sample No.		Sn-11						Sn-24						Sn-26			
Oxide wt %	1/4	1/5	3/10	3/11	3/15	1/7	1/12	2/2	2/8	3/1	3/2	1 / 1	1/10	1/12	1/25	1/16	1/22
SiO_2	0.64	0.78	0.80	0.79	0.85	0.04	0.10	0.04	0.03	0.51	0.52	0.72	0.25	0.63	0.27	0.47	0.41
P_2O_5	29.5	30.8	29.3	29.5	29.0	29.1	29.2	28.5	28.7	28.8	28.4	30.4	30.4	29.1	30.8	30.0	31.7
CaO	1.10	1.10	1.12	1.11	1.14	1.69	1.40	1.45	1.37	1.44	1.40	1.18	1.51	1.41	1.50	1.59	1.49
Y_2O_3	3.81	3.67	2.87	2.94	2.75	2.32	2.93	2.05	3.25	0.39	0.40	1.68	3.54	2.42	3.34	1.55	3.42
La_2O_3	11.6	12.3	11.7	11.7	12.1	13.8	13.7	14.2	14.6	17.1	17.1	12.5	12.5	13.4	12.5	13.3	12.4
Ce_2O_3	26.8	26.5	26.7	26.8	27.1	27.3	27.1	27.7	27.1	29.9	29.9	26.0	25.8	26.9	25.8	26.9	25.2
Pr_2O_3	3.43	3.42	3.64	3.59	3.63	3.25	3.40	3.37	3.33	3.17	3.26	3.62	3.46	3.45	3.40	3.41	3.61
Nd_2O_3	11.7	11.5	12.1	12.0	12.1	11.5	11.6	12.4	12.3	10.2	10.6	12.0	10.9	11.0	10.8	10.8	10.8
Sm_2O_3	2.25	2.24	2.36	2.31	2.33	1.70	1.90	1.93	1.94	0.91	1.01	2.24	2.29	2.20	2.32	2.22	2.37
Gd_2O_3	1.95	1.94	1.95	2.04	1.94	1.11	1.43	1.27	1.35	0.48	0.41	1.82	2.07	1.97	2.10	1.80	2.12
Dy_2O_3	0.38	0.41	0.32	0.41	0.33	0.00	0.15	0.10	0.24	0.00	0.00	0.13	0.41	0.30	0.42	0.05	0.63
PbO	0.12	0.13	0.14	0.14	0.13	0.22	0.16	0.18	0.15	0.17	0.17	0.18	0.17	0.18	0.16	0.43	0.42
ThO_2	5.71	5.59	6.31	6.17	5.76	6.23	5.43	5.46	5.24	7.18	7.10	7.39	5.71	5.80	5.70	6.54	5.40
UO_2	0.18	0.29	0.16	0.17	0.15	1.17	0.84	1.08	0.65	0.18	0.18	0.55	1.08	1.05	1.08	0.96	1.08
Total	99.17	100.67	99.47	99.67	99.31	99.43	99.34	99.73	100.25	100.43	100.45	100.41	100.09	99.81	100.19	100.02	101.05
Cations for 4 oxygen atoms																	
Si	0.026	0.030	0.030	0.030	0.034	0.003	0.005	0.003	0.010	0.022	0.022	0.028	0.010	0.027	0.012	0.019	0.016
P	0.976	0.987	0.976	0.976	0.969	0.990	0.990	0.990	0.979	0.963	0.969	0.990	0.990	0.947	0.990	0.990	1.000
Ca	0.045	0.043	0.045	0.045	0.048	0.073	0.061	0.063	0.061	0.063	0.061	0.049	0.062	0.061	0.062	0.067	0.061
Y	0.080	0.077	0.060	0.070	0.060	0.039	0.063	0.044	0.069	0.010	0.010	0.037	0.074	0.054	0.069	0.033	0.067
La	0.169	0.173	0.169	0.169	0.176	0.199	0.194	0.194	0.196	0.252	0.252	0.181	0.181	0.200	0.181	0.191	0.171
Ce	0.384	0.372	0.384	0.384	0.389	0.398	0.392	0.412	0.396	0.442	0.442	0.365	0.365	0.400	0.365	0.381	0.368
Pr	0.051	0.051	0.051	0.051	0.052	0.049	0.049	0.049	0.049	0.049	0.049	0.051	0.051	0.054	0.051	0.047	0.047
Nd	0.164	0.159	0.164	0.164	0.171	0.151	0.151	0.151	0.152	0.127	0.127	0.167	0.153	0.161	0.153	0.153	0.148
Sm	0.029	0.028	0.029	0.029	0.029	0.024	0.024	0.024	0.024	0.015	0.015	0.028	0.028	0.029	0.028	0.028	0.027
Gd	0.025	0.023	0.025	0.025	0.024	0.015	0.019	0.019	0.019	0.003	0.003	0.023	0.028	0.025	0.028	0.023	0.027
Dy	0.003	0.003	0.003	0.003	0.003	0.000	0.001	0.001	0.003	0.000	0.000	0.003	0.003	0.003	0.003	0.000	0.009
Pb	0.002	0.002	0.002	0.002	0.002	0.002	0.002	0.002	0.002	0.002	0.002	0.002	0.002	0.002	0.002	0.005	0.005
Th	0.052	0.048	0.055	0.054	0.052	0.059	0.051	0.051	0.049	0.066	0.064	0.065	0.051	0.054	0.051	0.058	0.047
UO_2	0.003	0.003	0.003	0.003	0.003	0.010	0.008	0.010	0.005	0.003	0.003	0.005	0.010	0.011	0.010	0.010	0.009
Total	2.009	1.999	1.996	2.005	2.012	2.012	2.009	2.012	2.014	2.017	2.019	1.994	2.008	2.028	2.005	2.005	2.002

prograde garnet through reaction 1. Variation in the modal abundances of some mineral phases in the pseudosection can be observed with changes in pressure and temperature. Garnet- and sillimanite-bearing mineral equilibria are stable at higher pressures, whereas cordierite-bearing mineral equilibria dominate at lower pressures in the pseudosection diagram. The decompression reaction inferred from petrographic observations and due to the decrease in pressure suggests reaction 6. The mineral equilibria of this specific bulk rock composition from Sonapahar exhibit peak metamorphic equilibria at higher pressures, followed by decompression at lower pressures. The mode isopleths of garnet are calculated to examine their nature with changes in *P–T* and other mineral phases in the equilibria. It is observed that in the narrow di-variant field

equilibria (grt–crd–bt–sil–ksp–pl–liq) with two tri-variant fields (grt–bt–sil–ksp–pl–liq and grt–crd–sil–ksp–pl–liq), the mode of garnet increases with increasing pressure. However, in the tri-variant mineral equilibria field (grt–bt–sil–ksp–pl–liq), which represents the peak mineral assemblage (cordierite absent), the mode of garnet increases with temperature.

6. Monazite dating

The EPMA (Th–U–Pb) dating technique is one of the most significant methods for constraining the ages of deformation and metamorphic events in different types of rocks (Suzuki & Adachi, 1991, 1998; Montel *et al.* 1996; Braun *et al.* 1998; Cocherie *et al.* 1998; Tickyj *et al.* 2004; Spear *et al.* 2009; Prabhakar, 2013). Monazite
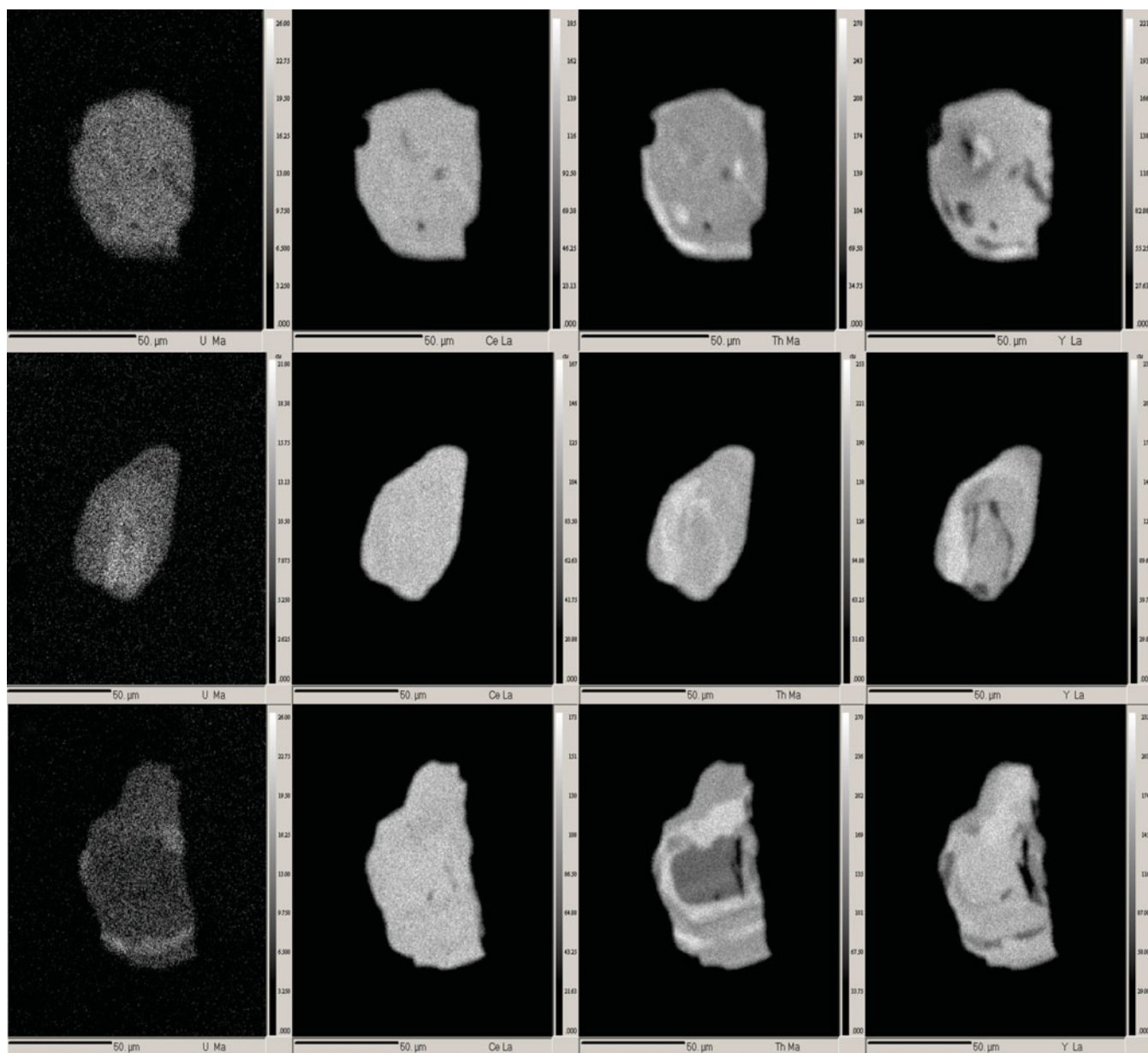
Fig. 4. X-ray elemental mapping of the three monazite grains G1, G2, G3 for U, Ce, Th and Y: (a) grain G1; (b) grain G2; (c) grain G3; prominent zoning is visible for Th.

is a light REE phosphate ((LREE) PO_4), rich in U and Th with little initial Pb (Parrish, 1990; Williams *et al.* 2007; Spear *et al.* 2009). Rapid accumulation of radiogenic lead (Pb^*) to a required level is possible and can be analysed with an electron microprobe (Montel *et al.* 1996). Thus, by assuming that the total Pb content is radiogenic, dating of monazite with an electron microprobe was performed based on the total abundances of Th, U and Pb (Suzuki & Adachi, 1991, 1994, 1998; Montel *et al.* 1996; Braun *et al.* 1998; Williams *et al.* 1999; Suzuki & Kato, 2008; Taylor *et al.* 2016; Hazarika *et al.* 2017).

6.a. Sample descriptions and U–Th–Pb systematics

Three samples Sn-11, Sn-24 and Sn-26 were taken from the Sonapahar granulites for detailed analysis. The analysed monazite grains occur as inclusions within garnet, cordierite and in the matrix. Monazite grains G1 and G2 occur as inclusions in the cordierite minerals of sample Sn-24, whereas grain G3 is present

within the core of a garnet in Sn-26. Monazite grain G4 contains only younger ages and is found in the matrix of the cordierite–spinel-bearing granulitic gneiss (Sn-11). The mineral chemistry of the monazites from all three samples is given in Table 6. Back-scattered electron (BSE) images are used to identify the monazite grains from the matrix and garnet. Large grains of monazite (100 μm) are commonly found in high-grade metamorphic rocks (Montel *et al.* 1996). All the monazite grains range in size from 50 to 80 μm (Fig. 4a–c). These three grains (G1, G2 and G3) were analysed for detailed study of elemental concentration variations and zoning with X-ray mapping to estimate the age. The monazite grains contain 3.32–7.20 wt % thorium (Th), 0.133–1.172 wt % uranium (U) and 0.101–0.513 wt % lead (Pb) (Table 7). The U and Th with Pb are grouped into the two types of huttonite and brabantite substitution. The brabantite substitution ($Th^{4+} + Ca^{2+} = 2REE^{3+}$; Rose, 1980) shows the compositional variation between Th (+Ca and Si) and Y (+HREE).

Table 7. EPMA dating age of Monazite grain of granulitic gneisses from the Sonapahar area

| Sn-26 & Sn-24 | | | | | | | | | | | | | | | | | |
UO_2	ThO_2	PbO	Y_2O_3	Age (Ma)	Age err	UO_2	ThO_2	PbO	Y_2O_3	Age (Ma)	Age err	UO_2	ThO_2	PbO	Y_2O_3	Age (Ma)	Age err
0.966	5.137	0.169	3.694	478	37	0.963	5.44	0.168	2.775	462	34	0.151	3.884	0.304	3.988	1570	101
1.080	5.190	0.175	3.872	472	35	0.609	5.49	0.153	3.118	480	37	0.165	3.653	0.281	3.998	1519	102
1.065	5.217	0.164	3.725	446	34	0.653	5.39	0.149	2.948	467	37	0.153	3.507	0.280	4.046	1577	107
0.526	6.131	0.157	3.189	469	39	0.916	6.29	0.184	2.355	466	32	0.138	4.036	0.312	3.743	1575	100
0.226	6.372	0.141	4.075	466	40	0.841	5.45	0.163	2.928	468	35	0.133	3.493	0.283	3.773	1626	110
0.712	6.275	0.169	2.368	461	37	0.848	5.33	0.171	2.411	495	37	0.151	3.662	0.281	3.932	1531	103
0.995	5.541	0.178	2.962	477	36	1.076	5.46	0.180	2.045	473	34	0.145	4.349	0.333	3.864	1568	96
0.961	5.794	0.180	2.567	473	36	0.799	5.39	0.156	2.835	459	35	0.302	6.093	0.472	3.119	1509	76
1.050	5.498	0.171	3.197	450	34	0.655	5.42	0.152	3.130	473	36	0.219	5.591	0.435	3.488	1560	83
1.062	5.209	0.169	3.608	458	35	0.841	5.25	0.163	2.461	480	37	0.232	5.971	0.454	3.095	1530	80
0.311	6.932	0.178	4.200	525	40	0.641	5.61	0.154	3.019	472	36	0.231	5.807	0.476	3.484	1637	83
0.309	5.690	0.157	4.241	549	45	0.660	5.61	0.148	3.175	450	35	0.305	6.203	0.513	3.342	1607	78
0.301	5.307	0.128	4.510	480	43	0.645	5.24	0.146	3.253	467	36	Weighted mean age 1571 ± 22 Ma (n = 18, MSWD = 1.2)					
0.262	5.230	0.122	4.430	472	44	0.636	5.16	0.143	3.409	464	37						
0.237	5.154	0.119	4.279	474	45	0.181	7.18	0.164	0.383	498	36	**Sn-11**					
0.230	5.349	0.121	4.008	466	44	0.177	7.10	0.172	0.397	525	37	0.305	4.543	0.101	2.686	428	46
0.306	6.493	0.155	4.198	485	40	0.192	7.11	0.162	0.392	492	36	0.384	4.489	0.103	3.454	422	43
0.303	6.156	0.149	4.296	489	41	0.170	7.02	0.164	0.382	509	37	0.201	5.801	0.127	4.251	463	40
0.282	5.759	0.134	4.336	474	42	0.179	7.20	0.167	0.373	505	36	0.180	5.711	0.119	3.792	447	40
0.206	5.403	0.122	3.721	474	45	Weighted mean age 478 ± 7 Ma (n = 55, MSWD = 1.7)						0.285	5.586	0.125	3.673	451	41
0.215	4.736	0.113	3.595	487	48							0.195	5.675	0.113	3.780	421	39
0.455	5.338	0.128	3.742	442	40	0.242	4.25	0.214	3.828	978	72	0.621	4.525	0.125	3.466	449	42
0.706	5.352	0.155	3.724	476	39	0.227	5.18	0.230	4.218	901	63	0.146	6.239	0.132	2.793	464	40
0.787	5.398	0.151	3.801	447	36	0.561	5.56	0.375	3.197	1158	62	0.140	6.357	0.129	2.865	444	39
0.877	5.301	0.153	3.805	440	36	0.960	6.54	0.431	1.548	1019	51	0.275	5.043	0.106	4.247	422	41
0.478	5.715	0.149	3.405	483	41	1.079	5.41	0.422	3.452	1075	55	0.537	4.833	0.123	2.978	439	42
0.714	6.092	0.173	2.129	484	38	1.034	5.83	0.380	2.069	945	47	0.145	6.354	0.137	2.711	471	40
0.860	5.561	0.177	3.599	497	37	0.763	5.43	0.253	3.270	1166	63	0.152	6.240	0.132	2.773	462	40
0.531	5.884	0.149	2.612	461	40	Weighted mean age 1034 ± 91 Ma (n = 7, MSWD = 2.9)						0.471	4.930	0.138	2.801	502	45
0.582	5.962	0.162	2.300	486	40							0.158	6.309	0.136	2.870	468	40
0.785	5.507	0.149	2.833	435	34	0.142	5.48	0.402	3.950	1539	85	0.170	6.165	0.141	2.935	493	41
0.997	5.006	0.192	2.217	545	38	0.158	3.32	0.280	4.175	1640	111	0.380	4.652	0.117	4.503	468	43
0.651	5.489	0.176	3.360	541	38	0.151	3.50	0.268	4.039	1521	105	0.254	5.847	0.132	3.136	467	41
0.654	5.316	0.151	3.017	478	37	0.136	3.58	0.269	4.045	1515	104	0.148	5.764	0.125	2.750	471	43
1.003	5.450	0.172	2.647	464	34	0.160	3.61	0.280	4.159	1531	103	0.667	3.678	0.125	4.059	502	47
1.172	6.230	0.219	1.811	512	33	0.143	3.82	0.301	4.070	1590	103	Weighted mean age 457 ± 11 Ma (n = 20, MSWD = 1.3)					

The variations in the brabantite versus huttonite exchange operation in monazite are represented on the plot of Th+U+Si versus REE+Y+P (Fig. 5a–d). Three samples were used for monazite dating viz. Sn-24 (Fig. 6a, b), Sn-26 (Fig. 6c) and Sn-11 (Fig. 6d). In

sample Sn-11, a monazite grain was examined in which Si varies from 0.01 to 0.04 pfu and Ca ranges from 0.04 to 0.06 pfu. From Sn-24, two monazite grains were selected for EPMA mineral dating; whereas Si contents are low compared to sample Sn-11, Ca is
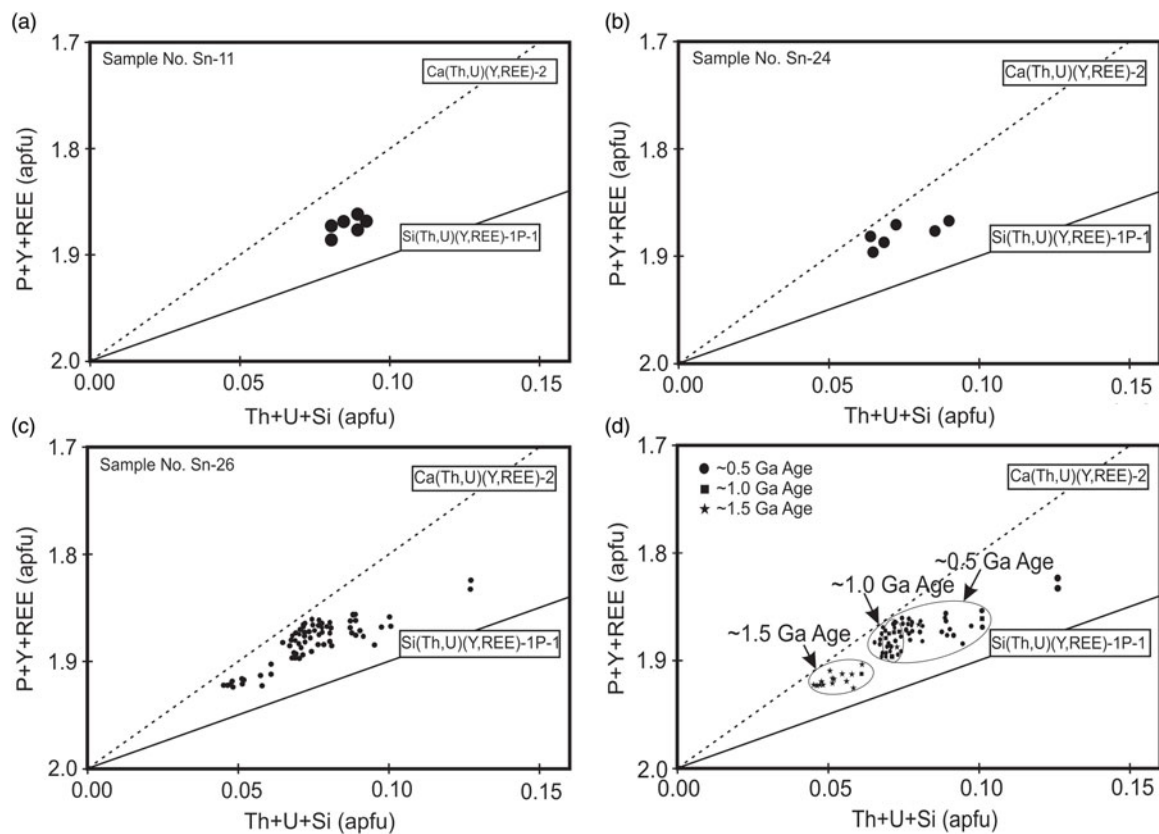
Fig. 5. Bivariate plot depicting the variation in composition of monazite from Sonapahar (SMGC). (a) For sample S-11, the monazite grain is enriched in brabantite (Th/U + Ca↔2REE) substitution. (b) For sample Sn-24, all grains are enriched in brabantite substitution. (c) For sample Sn-26, the monazite grain shows brabantite (Th/U + Ca↔2REE) substitution. (d) Bivariate plot showing the age distribution; ~1.5 Ga, ~1.0 Ga and ~0.5 Ga age domains are enriched in brabantite substitution as marked on the diagram.

slightly higher. In sample Sn-26, G3 contains Si from 0.01 to 0.04 pfu and Ca from 0.04 to 0.07 pfu. All the monazite grains from the different samples contain very much less Si than Ca. However, they provide an appropriate amount of Ca to quantify the brabantite (Th/U + Ca↔2REE) substitution. The G1, G2 and G3 monazite grains show compositional zoning patterns in X-ray mapping of the Th Mα element; however, G3 shows the most prominent zoning pattern (Figs 4c, 6c). There is no zoning pattern in the G4 monazite grain from Sn-11. Zonation of monazite in a metamorphic rock is a well-recognized phenomenon (Parrish, 1990; DeWolf *et al.* 1993; Zhu *et al.* 1997; Zhu & O'Nions, 1999; Bingen & van Breemen, 1998; Dahl *et al.* 2005; Mahan *et al.* 2006; Bhowmik *et al.* 2014; Taylor *et al.* 2016). The compositional zonation of monazite grains is important because the heterogeneity of monazite can reveal multistage growth and possible diffusion or partial recrystallization of Pb and Th (Scherrer *et al.* 2000; Taylor *et al.* 2014), and these processes can record several significant events in a single grain (Zhu & O'Nions, 1999; Spear & Pyle, 2002; Williams *et al.* 2007; Taylor *et al.* 2016).

7. Results

7.a. Monazite dating

The Th–U–Pb values from these three rock samples are given in Table 7. The probe analysis reveals that the ages of the rock range from Mesoproterozoic to Neoproterozoic, with older ages

(1571 ± 22 Ma) located in the cores and younger ages (478 ± 7 Ma) towards the rims of the monazite grains. A few spots from the monazite grains also yield intermediate ages between the older and younger ages, ranging from 1166 ± 63 to 901 ± 63 Ma (Fig. 6a–c). These calculated ages are well correlated with the ages reported by Chatterjee *et al.* (2007) and Yin *et al.* (2010). Weighted mean age distributions and cumulative histograms plotted using the Isoplot program (Ludwig, 2003) for the garnet-present (Sn-26) and garnet-absent (Sn-24) cordierite-bearing granulitic gneisses are presented in Figure 7a–c. The calculated weighted mean ages are 1571 ± 22 Ma (n = 18, MSWD = 1.2, probability = 0.22), 1034 ± 91 Ma (n = 7, MSWD = 2.9, probability = 0.007) and 478 ± 7 Ma (n = 55, MSWD = 1.7, probability = 0.001). Cordierite–spinel-bearing granulitic gneiss (Sn-11) has a single age domain (Fig. 7d), and the calculated weighted mean age is 457 ± 11 Ma (n = 20, MSWD = 1.3, probability = 0.16). The grains G1 and G2 from sample Sn-24 show ~1.0 Ga and 0.5 Ga age domains, whereas G3 from sample Sn-26 shows ~1.5 Ga, 1.0 Ga and ~0.5 Ga age domains; grain G4 from Sn-11 produced only a ~0.5 Ga age domain.

7.b. *P–T conditions of metamorphism*

The observed mineral equilibrium assemblages garnet–biotite–sillimanite–K-feldspar–plagioclase–liquid–quartz and garnet–cordierite–biotite–K-feldspar–plagioclase–liquid–quartz are obtained at the *P–T* range of 6.7 kbar/774 °C to 8.3 kbar/829 °C and at a low
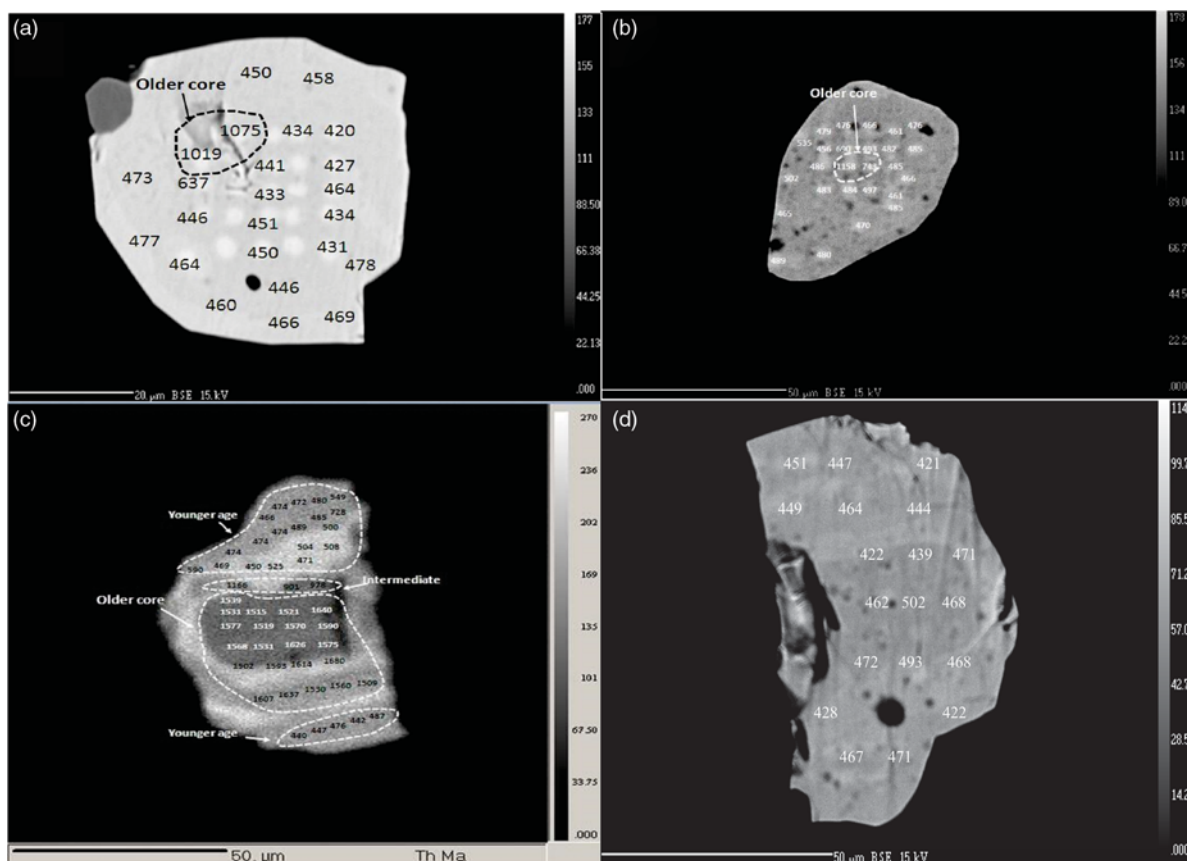
Fig. 6. Magnified BSE images of monazites showing chemical age (Ma) determined at spots on the monazite grains for each representative age. (a, b) Grains G1 and G2 of sample Sn-24 show an intermediate age at the core and the youngest age towards the rim. (c) Grain G3 of sample Sn-26 shows three distinct ages with the oldest age at the core, the youngest age towards the rim and the intermediate age located in the middle portion of the monazite grain. (d) Grain G4 of Sn-11 shows only the youngest age throughout the monazite grain.

pressure of 5.9 kbar/754 °C, respectively, in the NCKFMASH system. The mineral equilibria of this specific bulk rock composition from Sonapahar exhibit peak metamorphic equilibrium at higher pressure, followed by decompression to lower pressure. This type of pseudosection diagram, which represents the equilibria experienced by a particular bulk composition, is important in representing the mineral equilibria and allows us to decipher the mineral assemblages and relationships observed in the rock (White *et al.* 2001). The equilibrium mineral phases calculated for the Sonapahar granulitic gneisses lie in the *P–T* range from 5.9 kbar/754 °C to 8.3 kbar/829 °C in the NCKFMASH system (Fig. 8). The *P–T* condition for spinel-bearing equilibria is not discussed in Figure 8; therefore, the *P–T* conditions of all rock types of the Sonapahar granulitic gneisses are estimated through THERMOCALC v.3.33 using the internally consistent dataset of Powell & Holland (1988). The *P–T*$_{\mathrm{av}}$ mode was calculated with phases involving garnet, biotite, sillimanite, K-feldspar, plagioclase, quartz, rutile, ilmenite; cordierite, spinel, magnetite, biotite, sillimanite, K-feldspar, quartz; and garnet, cordierite, biotite, K-feldspar, plagioclase, quartz, ilmenite, rutile at 0.5 H$_2$O activity. The result of these three types of coexisting phases is presented in Tables 8–10. The *P–T*$_{\mathrm{av}}$ estimates are consistent with the *P–T* estimate of mineral equilibria from the pseudosection (Fig. 8). A metamorphic evolution *P–T* path (Fig. 9) is deduced on the basis of textural relationships, metamorphic reactions, coexisting mineral phases and the NCKFMASH pseudosection. The pressure and

temperature conditions of the granulitic gneiss emphasize the following points:

(a) The peak mineral assemblage garnet–biotite–K-feldspar–plagioclase–sillimanite–quartz–rutile–ilmenite–liquid formed during M$_1$ (peak) metamorphism in the *P–T* range from 7.5 kbar/677 °C to 8.2 kbar/713 °C with an average *P–T* of 7.9 ± 0.8 kbar/697 ± 41 °C.

(b) Cordierite–spinel-bearing granulitic gneiss includes the mineral assemblage cordierite–spinel–sillimanite–biotite–magnetite–K-feldspar–plagioclase–quartz–ilmenite–liquid, in which the *P–T* conditions range from 5.8 kbar/815 °C to 5.9 kbar/817 °C with an average *P–T* of 5.9 ± 1.9 kbar/816 ± 93 °C.

(c) The *P–T* values for the retrograde mineral assemblage garnet–cordierite–biotite–sillimanite–plagioclase–K-feldspar–quartz–rutile–ilmenite–liquid, formed during M$_2$ (post-peak) metamorphism, lie in the *P–T* range from 3.9 kbar/701 °C to 4.2 kbar/715 °C with an average *P–T* of 4.0 ± 0.8 kbar/706 ± 54 °C.

The *P–T* values of the granulitic gneiss trace a clockwise *P–T* path (Fig. 9) during the maximum pressure, which is achieved during the M$_1$ (peak) metamorphic stage represented by peak coexisting mineral assemblages of the prograde garnet-forming
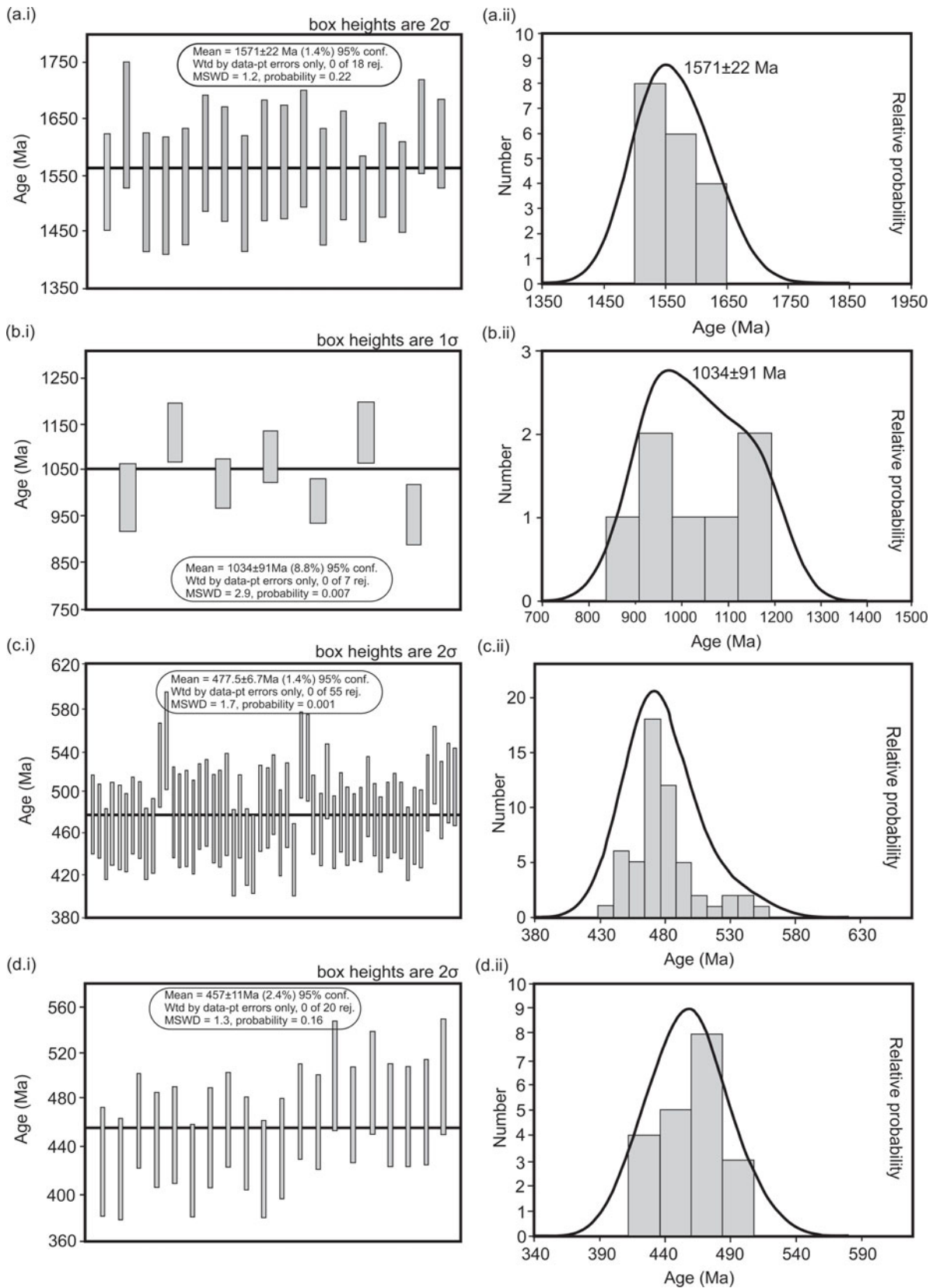
Fig. 7. Chemical age of monazite from Sonapahar granulitic gneisses (Sn-24 and Sn-26). Isoplot weighted mean age distributions with cumulative histograms (Ludwig, 2003): (a) older age; (b) intermediate age; (c) younger age; (d) younger age of cordierite–spinel-bearing granulitic gneisses (Sn-11).

Table 8. Average *P–T* condition for garnet–cordierite–biotite–sillimanite–plagioclase–K-feldspar–ilmenite–quartz–melt at H₂O activity of 0.5

aH₂O		0.5		Average
T °C	715	701	703	706
s.d. (*T*)	44	59	58	53.7
P kbar	4.2	3.9	3.9	4.0
s.d. (*P*)	0.7	0.9	0.9	0.8
correl.	0.857	0.850	0.856	0.854
Sig fit	0.83	1.36	1.31	1.66

Table 9. Average *P–T* condition for garnet–biotite–sillimanite–plagioclase–K-feldspar–ilmenite–quartz–rutile–melt at H₂O activity of 0.5

| aH₂O		0.5			Average
T °C	713	699	700	677	697
s.d. (*T*)	44	41	41	38	41
P kbar	8.2	7.9	7.8	7.5	7.9
s.d. (*P*)	0.8	0.8	0.8	0.7	0.8
correl.	0.607	0.599	0.600	0.586	0.598
Sig fit	0.83	0.62	0.69	0.79	0.73
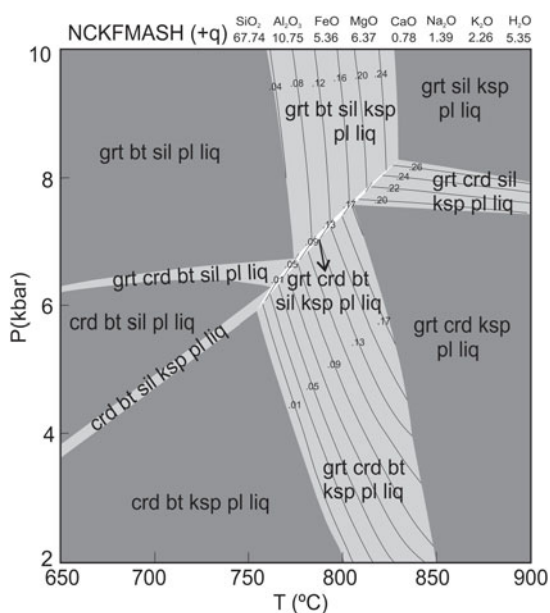
Fig. 8. Garnet mode isopleths on NCKFMASH *P–T* pseudosection for Sonapahar granulitic gneiss (Sn-26) depict calculated mineral equilibria for the mineral assemblage grt–crd–pl–sil–kfs–bt–q–liq (mineral abbreviations from Whitney & Evans, 2010).

reaction at the *P–T* condition of 8.2 kbar/713 °C. With further decompression (3.9 kbar/701 °C) garnet–sillimanite–biotite–quartz and spinel–quartz break down to form cordierite during the M₂ (post-peak) metamorphic stage; this is the dominant metamorphic event in the study area. The metamorphic evolution of the granulitic gneisses progresses through an isothermal decompression path.

Table 10. Average *P–T* condition for cordierite–spinel–biotite–magnetite–sillimanite–plagioclase–K-feldspar–ilmenite–quartz–melt at H₂O activity of 0.5

aH₂O		0.5	Average
T °C	817	815	816
s.d. (*T*)	101	84	93
P kbar	5.9	5.8	5.9
s.d. (*P*)	2.0	1.7	1.9
correl.	0.887	0.885	0.886
Sig fit	1.84	1.50	1.67
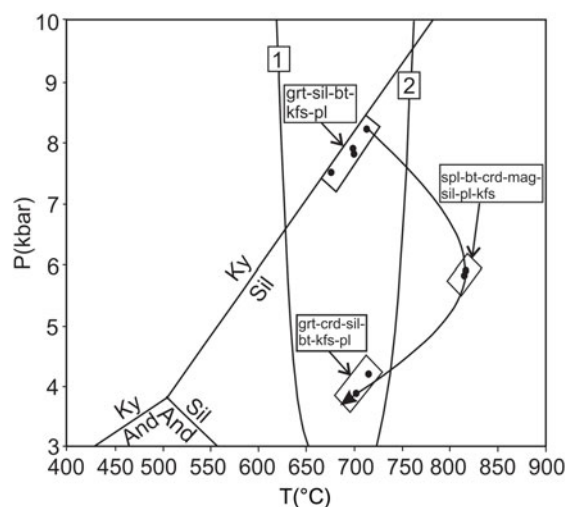
Fig. 9. Clockwise retrograde/decompression pressure–temperature (*P–T*) path at 0.5 H₂O activity (using internally consistent dataset of Holland & Powell, 1998) shown on *P–T* diagram indicating the metamorphic evolution of granulitic gneisses in the study area based on geothermobarometry, the pseudosection and reactions from textural relationships.

8. Discussion

Chemical dating of monazite grains from the Sonapahar area was performed because it has been successfully applied to constrain the ages of deformation and metamorphic events. Three monazite-bearing granulitic samples were analysed, yielding three distinct ages from the prominent zoning of the monazite grains (478 ± 7 Ma; 1034 ± 91 Ma; 1571 ± 22 Ma). The growth stages of monazite are recognized when an individual grain contains distinct age domains in the core and the rim. The distinct compositional zoning domains in grain G3 from sample Sn-26 are one of the most important characteristics of the monazite, because these domains can be interpreted with regard to the generation of monazite growth (Williams *et al.* 2006 and references therein). The monazite grain G3, which occurs as an inclusion within a garnet core, provides three different age domains (478 ± 7 Ma; 1034 ± 91 Ma; 1571 ± 22 Ma) that may be due to the effect of three different types of tectonic activity that occurred in the study area. Monazite is also found as inclusions in cordierite, suggesting that the younger age of ~0.5 Ga was dominant during the Pan-African orogeny when decompression occurred in the cordierite-bearing assemblages of the granulitic gneisses. A number of studies of the monazite population and single grains of monazite in metamorphic rocks have noted that monazite may grow stepwise along the prograde path of

a *P–T* loop. The prograde monazite grains are generated during the formation of melt, whereas post-peak monazite grains are recrystallization products of pre-existing grains (Johnson *et al.* 2015). Monazite also develops stepwise during decompression (Franz *et al.* 1996; Pyle & Spear, 2003; Foster *et al.* 2004; Gibson *et al.* 2004). The Sonapahar metapelitic granulites reveal the post-S_1/pre-S_2 stage of metamorphism at ∼1.5 Ga with poorly preserved 1.0–1.3 Ga ages in the rim of a monazite grain in contact with a syn-S_2 feature, which may be due to an extended period of cooling along the retrograde metamorphic path, and the more significant occurrence of 649–524 Ma ages, both of which are considered post-S_2 stages of metamorphism (Chatterjee *et al.* 2007, 2011; Chatterjee, 2017). The analysis of the zoned monazite suggests that the three distinct ages (1571 ± 22 Ma; 1034 ± 91 Ma; 478 ± 7 Ma) from the Mesoproterozoic to Neoproterozoic can be correlated with the ages of peak and two post-peak metamorphic stages that must have influenced the Sonapahar granulites, which is similar to the conclusions of Chatterjee *et al.* (2007). It is predicted that the dominant metamorphic event is the Pan-African orogeny (478 ± 7 Ma), which might affect the rim portion of the monazite grains, because the '1034 Ma age' is poorly obtained in the analytical data. The crust formation of the Meghalaya massif started during Archaean time and experienced a protracted and episodic evolution (Bidyananda & Deomurari, 2007). The Mesoproterozoic age of 1571 ± 22 Ma is considered peak metamorphism, during which prograde garnet is formed through reaction 1, which might be related to the maximum pressure conditions in the granulite of the study area. Although the intermediate age of 1034 ± 91 Ma is poorly preserved, it may be related to the Grenvillian orogenic event during the formation of the Rodinia supercontinent and represents the post-peak metamorphic stage at Sonapahar, or it may be a mixing artefact of the Grenvillian and Pan-African orogenies. The youngest age (478 ± 7 Ma), which is associated with the Pan-African orogeny, suggests that the Sonapahar granulites were part of an accretionary event of the Gondwana supercontinent; it also correlates with the amphibolite- to granulite-facies metamorphism of the Pinjarra orogenic belt and represents the dominant post-peak (M_2) metamorphism in the Sonapahar area.

The SMGC is an isolated part of the Indian Peninsula (Evans, 1964), the northern extension of the Eastern Ghats Mobile Belt (Crawford, 1974) and the NE extension of the CGC (Desikachar, 1974). Recent studies in the SMGC (Bidyananda & Deomurari, 2007; Chatterjee *et al.* 2007, 2011; Yin *et al.* 2010; Chatterjee, 2017; Borah *et al.* 2019) and CGC (Chatterjee *et al.* 2008, 2010; Maji *et al.* 2008; Sanyal & Sengupta, 2012; Mukherjee *et al.* 2017, 2018; Kumar & Dwivedi, 2019) have observed the same geochronological age from the basement of the SMGC and the CGC and established a significant relationship between the Mesoproterozoic metamorphic terrain and the CGC. Similar coeval metamorphism has been reported in the Proterozoic gneissic complexes of central India during 1.61–1.57 Ga where supra-crustal granulites were metamorphosed under ultra-high-temperature conditions along the southern margin of the CITZ (Bhowmik *et al.* 2005, 2014). These authors concluded that collisional tectonism occurred between the SIB and NIB at 1.57–1.54 Ga when the oceanic lithospheric of the SIB was subducted beneath the NIB to form an island arc, whereas episodic magmatic injection intruded in the back-arc to form the granulite-facies rocks. Similar lithological and metamorphic trends are reported in the SMGC, which indicates the possibility that the northern Garo Hills rocks formed in a back-arc environment (Chatterjee, 2017).

9. Conclusions

Petrological and mineralogical data reveal that three distinct ages (1571 ± 22 Ma; 1034 ± 91 Ma and 478 ± 7 Ma) from the Mesoproterozoic to Neoproterozoic can be correlated with peak and two post-peak stages of metamorphism that must have influenced the Sonapahar granulitic rocks. Stable mineral equilibria are calculated for the NCKFMASH system with the peak assemblage stable in the *P–T* range of 6.7 kbar/774 °C to 8.3 kbar/829 °C. The *P–T*$_{av}$ values of the granulitic gneiss trace a clockwise *P–T* path. The maximum pressure and moderate temperature were achieved during the peak (M_1) metamorphic stage represented by peak mineral assemblages of the prograde garnet-forming reaction (8.2 kbar/713 °C), followed by decompression reactions through which garnet–sillimanite and spinel–quartz broke down to form cordierite during the post-peak (M_2) metamorphic stage (3.9 kbar/701 °C). The granulites of Sonapahar were exhumed along an isothermal decompression path. The oldest age of 1571 ± 22 Ma is considered to represent a peak metamorphic assemblage. The intermediate age of 1034 ± 91 Ma may be a mixing artefact and represents post-peak metamorphism, and the most dominant youngest age (478 ± 7 Ma) from the granulitic gneisses of the study area, related to the Pan-African orogeny, suggests that the Sonapahar granulites were part of the accretionary process of the Gondwana supercontinent and represents the dominant post-peak (M_2) metamorphism. The Pan-African orogeny overprinted the evidence of a mixing artefact in Sonapahar, which is dominated by post-peak (M_2) metamorphic events. The Sonapahar granulitic gneisses of the Shillong Plateau contain Mesoproterozoic ages of 1571 Ma in the core parts of monazite grains and 1034 Ma in the intermediate portions of the monazite grains (mixing artefact); this evidence strongly shows the extension of the CITZ and Eastern Ghats Mobile Belt in the Shillong Plateau.

References

Acharyya SK, Mitra ND and Nandy DR (1986) Regional geology and tectonic setting of North-East India and Adjoining region. In *Geology of Nagaland Ophiolite. G. B. Ghosh Commemorative Volume (A Compilation of Research Papers on Nagaland Ophiolite)* (eds ND Mitra, SK Acharyya, AK Datta, S Ghosh, DR Nandy, DK Roy, KT Vidyadharan, P Venktaraman, RK Srivastava, S Bhattacharyya, A Joshi, SK Jena and HK Goswami), pp. 6–12. Geological Survey of India, Memoir 119.

Anon (1974) Geology and mineral resources of the states of India – Assam and adjoining states. *Geological Survey of India, Miscellaneous Publication* **30**, 1–24.

Banerjee AK (1955) A petrological note on the metamorphites around Sonapahar in the Khasi hills, Assam. *Journal of University of Guwahati* **4**, 201–16.

Bhowmik SK, Sarbadhikari AB, Spiering B and Raith M (2005) Mesoproterozoic reworking of Palaeoproterozoic ultrahigh-temperature granulites in the Central Indian Tectonic Zone and its implications. *Journal of Petrology* **46**, 1085–119.

Bhowmik SK, Wilde SA, Bhandari A, Pal T and Pant NC (2012) Growth of the Greater Indian landmass and its assembly in Rodinia: geochronological evidence from the Central Indian Tectonic Zone. *Gondwana Research* **22**, 54–72.

Bhowmik SK, Wilde SA, Bhandari A and Sarbadhikari AB (2014) Zoned monazite and zircon as monitors for the thermal history of granulite terranes: an example from the Central Indian Tectonic Zone. *Journal of Petrology* **55**, 585–621.

Bidyananda M and Deomurari MP (2007) Geochronological constraints on the evolution of Meghalaya massif, northeastern India: an ion microprobe study. *Current Science* **93**, 1620–3.

Bingen B and van Breemen O (1998) U–Pb monazite ages in amphibolite to granulite-facies orthogneiss reflect hydrous mineral breakdown reaction: Sveconorwegian Province of SW Norway. *Contributions to Mineralogy and Petrology* **132**, 336–5.

Biswal TK, de Waele B and Ahuja H (2007) Timing and dynamics of the juxtaposition of the Eastern Ghats mobile belt against the Bhandara craton, India: a structural and zircon U–Pb SHRIMP study of the fold-thrust belt and associated nepheline syenite plutons. *Tectonics* **26**, 1–21.

Boger SD, Carson CJ, Wilson CJL and Fanning CM (2000) Neoproterozoic deformation in the Radok Lake region of the northern Prince Charles Mountains, East Antarctica; evidence for a single protracted orogenic event. *Precambrian Research* **104**, 1–24.

Borah P, Hazarika P, Mazumdar AC and Rabha M (2019) Monazite and xenotime U–Th–Pb$_{total}$ ages from basement rocks of the (central) Shillong–Meghalaya Gneissic Complex, Northeast India. *Journal of Earth System Science* **128**, 68, doi: 10.1007/s12040-019-1085-x.

Braun I, Montel JM and Nicollet C (1998) Electron microprobe dating of monazites from high-grade gneisses and pegmatites of the Kerala Khondalite Belt, Southern India. *Chemical Geology* **146**, 65–85.

Chatterjee N (2017) Constraints from monazite and xenotime growth modelling in the MnCKFMASH-PYCe system on the *P–T* path of a metapelite from Shillong-Meghalaya Plateau: implications for the Indian shield assembly. *Journal of Metamorphic Geology* **35**, 393–412.

Chatterjee N, Banerjee M, Bhattacharya A and Maji AK (2010) Monazite chronology, metamorphism-anatexis and tectonic relevance of the mid-Neoproterozoic Eastern Indian Tectonic Zone. *Precambrian Research* **179**, 99–120.

Chatterjee N, Bhattacharya A, Duarah BP and Mazumdar AC (2011) Late Cambrian reworking of Palaeo-Mesoproterozoic granulites in Shillong–Meghalaya Gneissic Complex (Northeast India): evidence from PT pseudosection analysis and monazite chronology and implications for East Gondwana assembly. *Journal of Geology* **119**, 311–30.

Chatterjee N, Crowley JL and Ghose NC (2008) Geochronology of the 1.55 Ga Bengal anorthosite and Grenvillian metamorphism in the Chotanagpur Gneissic Complex, eastern India. *Precambrian Research* **161**, 303–16.

Chatterjee N, Mazumder AC, Bhattacharya A and Saikia RR (2007) Mesoproterozoic granulites of the Shillong-Meghalaya Plateau: evidence of westward continuation of the Prydz Bay Pan-African suture into Northeastern India. *Precambrian Research* **152**, 1–26.

Cocherie A, Legendre O, Peucat JJ and Kouamelan A (1998) Geochronology of polygenic monazites constrained by in situ electron microprobe Th-U-total Pb determination: implications for Pb behavior in monazite. *Geochimica et Cosmochimica Acta* **62**, 2475–97.

Collins AS, Santosh M, Braun I and Clark C (2007) Age and sedimentary provenance of the southern granulites, South India: U-Th-Pb SHRIMP secondary ion mass spectrometry. *Precambrian Research* **155**, 125–38.

Crawford AR (1974) Indo-Antarctica, Gondwanaland and pattern of the distortion of a granulite belt. *Tectonophysics* **22**, 141–57.

Dahl PS, Hamilton MA, Jercinovic MJ, Terry MP, Williams ML and Frei R (2005) Comparative isotopic and chemical geochronometry of monazite, with implications for U-Th-Pb dating by electron microprobe: an example from metamorphic rocks of the eastern Wyoming Craton (U.S.A.). *American Mineralogist* **90**, 619–38.

Dalziel IWD (1991) Pacific margins of Laurentia and East Antarctica–Australia as a conjugate rift pair: evidence and implications for an Eocambrian supercontinent. *Geology* **19**, 598–601.

Desikachar SV (1974) A review of the tectonic and geological history of eastern India in terms of plate tectonic theory. *Journal of the Geological Society of India* **15**, 137–49.

DeWolf CP, Belshaw N and O'Nions RK (1993) A metamorphic history from micron-scale ^{207}Pb/ ^{206}Pb chronometry of Archean monazite. *Earth and Planetary Science Letters* **120**, 207–20.

Dwivedi SB (2011) Geodynamic evolution of Mesoproterozoic granulites of Meghalaya: evident from geothermobarometry, P-T path and P-T pseudo-section. In *Geodynamics, Sedimentation and Biotic Response in the Context of India–Asia Collision* (ed. RP Tiwari), pp. 85–101. Geological Society of India, Memoir 77.

Dwivedi SB and Theunuo K (2011) Two-pyroxene bearing granulites from Patharkhang, Shillong-Meghalaya Gneissic Complex (SMGC). *Current Science* **100**, 100–5.

Dwivedi SB and Theunuo K (2013) Petrology and geochemistry of metapelites and basic granulite from Sonapahar region of Shillong Meghalaya Gneissic Complex, North East India. *Journal of the Geological Society of India* **81**, 55–766.

Dwivedi SB and Theunuo K (2017) Occurrence of wagnerite in Mg-Al granulites of Sonapahar Meghalaya. *Journal of Earth System Science* **126**, 52.

Evans P (1964) The tectonic framework of Assam. *Journal of the Geological Society of India* **5**, 80–96.

Fitzsimons ICW (2000) A review of tectonic events in the East Antarctic shield and their implications for Gondwana and earlier supercontinents. *Journal of African Earth Sciences* **31**, 3–23.

Fitzsimons ICW (2003) Proterozoic basement provinces of southern and southwestern Australia, and their correlation with Antarctica. In *Proterozoic East Gondwana: Supercontinent Assembly and Breakup 206* (eds M Yoshida, BF Windley and S Dasgupta), pp. 93–130. Geological Society of London, Special Publication no. 206.

Foster G, Gibson HD, Parrish R, Horstwood M, Fraser J and Tindle A (2004) Textural, chemical and isotopic insights into the nature and behaviour of metamorphic monazite. *Chemical Geology* **191**, 183–207.

Franz G, Andrehs G and Rhede D (1996) Crystal chemistry of monazite and xenotime from Saxothuringian–Moldanubian metapelites, NE Bavaria, Germany. *European Journal of Mineralogy* **8**, 1097–118.

Ghosh AMN (1952) A preliminary note on the gneissic complex of Nongmaweit-Rambrai-Nongstoin plateau, Khasi hills, Assam. *Records in Geological Survey of India* **82**, 308–14.

Ghosh AMN and Saha AK (1954) On certain sapphirine-bearing rocks from the Khasi Hills, Assam. *Records in Geological Survey of India* **83**, 445.

Ghosh JG, de Wit MJ and Zartman RE (2004) Age and tectonic evolution of Neoproterozoic ductile shear zones in the southern granulite terrain of India, with implications for Gondwana studies. *Tectonics* **23**, 1–38.

Gibson HD, Carr SD, Brown RL and Hamilton MA (2004) Correlations between chemical and age domains in monazite, and metamorphic reactions involving major pelitic phases: an integration of ID-TIMS and SHRIMP geochronology with Y-Th-U X-ray mapping. *Chemical Geology* **211**, 237–60.

Golani PR (1991) Nongchram fault: a major dislocation zone from western Meghalaya. *Journal of the Geological Society of India* **37**, 31–8.

Gupta RP and Sen AK (1988) Imprints of the Ninety-East Ridge in the Shillong-Plateau, Indian shield. *Tectonophysics* **154**, 335–41.

Harijan N, Sen AK, Sarkar S, Das JD and Kanungo DP (2003) Geomorpho-tectonics around Sung valley carbonatite complex, Shillong plateau, NE India: remote sensing and GIS approach. *Journal of the Geological Society of India* **62**, 103–9.

Hazarika P, Mishra B, Ozha MK and Pruseth KL (2017) An improved EPMA analytical protocol for U–Th–Pb$_{total}$ dating in xenotime: age constraints from polygenetic Mangalwar Complex, Northwestern India. *Chemie der Erde Geochemistry* **77**, 69–79.

Hoffman PF (1991) Did the breakout of Laurentia turn Gondwanaland inside out? *Science* **252**, 1409–12.

Holland TJB and Powell R (1998) An internally consistent thermodynamic dataset for phases of petrological interest. *Journal of Metamorphic Geology* **16**, 309–43.

Holland TJB and Powell R (2003) Activity–composition relations for phases in petrological calculations: an asymmetric multi component formulation. *Contributions to Mineralogy and Petrology* **145**, 492–501.

Johnson TE, Clark C, Taylor RJM, Santosh M and Collins AS (2015) Prograde and retrograde growth of monazite in migmatites: an example from the Nagercoil Block, southern India. *Geoscience Frontiers* **6**, 373–87.

Kelsey DE, Clark C and Hand M (2008) Thermobarometric modelling of zircon and monazite growth in melt-bearing systems: examples using model metapelitic and metapsammitic granulites. *Journal of Metamorphic Geology* **26**, 199–212.

Kumar RR and Dwivedi SB (2019) EPMA monazite geochronology of the granulites from Daltonganj, Eastern India and its correlation with Rodinia Supercontinent. *Journal of Earth System Science* **128**, 1–22.

Kumar S, Rino V, Hayasaka Y, Kimura K, Raju S, Terada K and Pathak M (2017) Contribution of Columbia and Gondwana supercontinent assembly and growth-related magmatism in the evolution of the Meghalaya Plateau and the Mikir Hills, Northeast India: constraints from U–Pb SHRIMP zircon geochronology and geochemistry. *Lithos* **277**, 356–77.

Lal RK, Ackermand D, Seifert F and Haldar SK (1978) Chemographic relationships in sapphirine-bearing rocks from Sonapahar, Assam, India. *Contributions to Mineralogy and Petrology* **67**, 169–87.

Li ZX, Bogdanova SV, Collins AS, Davidson A, Waele BD, Ernst RE, Fitzsimons ICW, Fuck RA, Gladkochub DP, Jacobs J, Karlstrom KE, Lu S, Natapov LM, Pease V, Pisarevsky SA, Thrane K and Vernikovsky V (2008) Assembly, configuration, and break-up history of Rodinia: a synthesis. *Precambrian Research* **160**, 179–210.

Ludwig KR (2003) *User's Manual for Isoplot 3.00: A Geochronological Toolkit for Microsoft Excel.* Berkeley Geochronology Center, Special Publication no. 4.

Mahan KH, Goncalves P, Williams ML and Jercinovic MJ (2006) Dating metamorphic reactions and fluid flow: application to exhumation of high-P granulites in a crustal-scale shear zone, western Canadian Shield. *Journal of Metamorphic Geology* **24**, 193–217.

Maji AK, Goon S, Bhattacharya A, Mishra B, Mahato S and Bernhardt HJ (2008) Proterozoic polyphase metamorphism in the Chhotanagpur gneissic complex (India) and implication for trans-continental Gondwanaland correlation. *Precambrian Research* **162**, 385–402.

Mazumdar SK (1976) A summary of the Precambrian geology of the Khasi Hills, Meghalaya. *Geological Survey of India, Miscellaneous Publication* **23**, 311–34.

Mezger K and Cosca MA (1999) The thermal history of the Eastern Ghats Belt (India) as revealed by U-Pb and ^{40}Ar/^{39}Ar dating of metamorphic and magmatic minerals: implications SWEAT correlation. *Precambrian Research* **94**, 251–71.

Mishra DC, Singh B, Tiwari VM, Gupta SB and Rao MBSV (2000) Two cases of continental collision and related tectonics during the Proterozoic period in India: insight from gravity modelling constrained by seismic and magnetotelluric studies. *Precambrian Research* **99**, 149–69.

Montel JM, Foret S, Veschambre M, Christian N and Provost A (1996) Electron microprobe dating of monazite. *Chemical Geology* **131**, 37–53.

Moores EM (1991) Southwest U.S.–East Antarctic (SWEAT) connection: a hypothesis. *Geology* **19**, 425–28.

Mukherjee S, Dey A, Ibanez-Mejia M, Sanyal S and Sengupta P (2018) Geochemistry, U–Pb geochronology and Lu–Hf isotope systematics of a suite of ferroan (A-type) granitoids from the CGGC: evidence for Mesoproterozoic crustal extension in the East Indian shield. *Precambrian Research* **305**, 40–63.

Mukherjee S, Dey A, Sanyal S, Ibanez-Mejia M, Dutta U and Sengupta P (2017) Petrology and U–Pb geochronology of zircon in a suite of charnockitic gneisses from parts of the Chhotanagpur Granite Gneiss Complex (CGGC): evidence for the reworking of a Mesoproterozoic basement during the formation of the Rodinia supercontinent. In *Crustal Evolution of India and Antarctica: The Supercontinent Connection* (eds NC Pant and S Dasgupta), pp. 197–231. Geological Society of London, Special Publication no. 457.

Naganjaneyulu K and Santosh M (2010) The Central India Tectonic Zone: a geophysical perspective on continental amalgamation along a Mesoproterozoic suture. *Gondwana Research* **18**, 547–64.

Nandy DR (1986) Tectonics, seismicity and gravity of Northeastern India and adjoining region. In *Geology of Nagaland Ophiolite. G. B. Ghosh Commemorative Volume (A Compilation of Research Papers on Nagaland Ophiolite)* (eds ND Mitra, SK Acharyya, AK Datta, S Ghosh, DR Nandy, DK Roy, KT Vidyadharan, P Venktaraman, RK Srivastava, S Bhattacharyya, A Joshi, SK Jena and HK Goswami), pp. 13–16. Geological Survey of India Memoir 119.

Nandy DR (2001) *Geodynamics of the Northeastern India and the Adjoining Region.* Kolkata: ABC Publications, 209 pp.

Parrish RR (1990) U–Pb dating of monazite and its application to geological problem. *Canadian Journal of Earth Sciences* **27**, 1431–50.

Powell R and Holland TJB (1988) An internally consistent thermodynamic dataset with uncertainties and correlations; 3, Application to geobarometry, worked examples and a computer program. *Journal of Metamorphic Geology* **6**, 173–204.

Prabhakar N (2013) Resolving poly-metamorphic Paleoarchean ages by chemical dating of monazites using multi-spectrometer U, Th and Pb analyses and sub-counting methodology. *Chemical Geology* **347**, 255–70.

Pyle JM and Spear FS (2003) Yttrium zoning in garnet: coupling of major and accessory phases during metamorphic reactions. *Geological Materials Research* **1**, 1–49.

Rajendran CP, Rajendran K, Duarah BP, Baruah S and Earnest A (2004) Interpreting the style of faulting and paleoseismicity associated with the 1897 Shillong, northeast India, earthquake: Implications for regional tectonism. *Tectonics* **23**, 1–12.

Ramesh DS, Kumar MR, Devi EU, Raju PS and Yuan X (2005) Moho geometry and upper mantle images of northeast India. *Geophysical Research Letters* **32**, 14301–4.

Rogers JJW and Santosh M (2002) Configuration of Columbia, a Mesoproterozoic supercontinent. *Gondwana Research* **5**, 5–22.

Rose D (1980) Brabantite, CaTh[PO$_4$]$_2$, a new mineral of the monazite group. *Neues Jahrbuch für Mineralogy, Monatshefte* **6**, 247–57.

Sanyal S and Sengupta P. (2012) Metamorphic evolution of the Chhotanagpur granite gneiss complex of the East Indian Shield: current status. In *Palaeoproterozoic of India* (eds Mazumder R and D Saha), pp. 117–45. Geological Society of London, Special Publication no. 365.

Scherrer NC, Engi M, Gnos E, Jakob V and Liechti A (2000) Monazite analysis; from sample preparation to microprobe age dating and REE quantification. *Schweizerische mineralogische und petrographische Mitteilungen (Bulletin suisse de mineralogie et pétrographie)* **80**, 93–105.

Sengupta PR and Agarwal NK (1998) The tectonic segments of Northeastern India and associated gold mineralisation. *Journal of the Geological Society of India* **52**, 549–56.

Spear FS and Pyle JM (2002) Apatite, monazite, and xenotime in metamorphic rocks. *Reviews in Mineralogy and Geochemistry* **48**, 293–335.

Spear FS, Pyle JM and Cherniak D (2009) Limitations of chemical dating of monazite. *Chemical Geology* **266**, 218–30.

Srivastava RK, Guarino V, Wu FY, Melluso L and Sinha AK (2019) Evidence of sub-continental lithospheric mantle sources and open-system crystallization processes from *in-situ* U–Pb ages and Nd–Sr–Hf isotope geochemistry of the Cretaceous ultramafic-alkaline-(carbonatite) intrusions from the Shillong Plateau, north-eastern India. *Lithos* **330–331**, 108–19.

Suzuki K and Adachi M (1991) Precambrian provenance and Silurian metamorphism of the Tsubonasawa paragneiss in the South Kitakami terrane, Northeast Japan, revealed by the Chemical Th–U–total Pb-isochron ages of monazite, zircon and xenotime. *Geochemical Journal* **25**, 357–76.

Suzuki K and Adachi M (1994) Middle Precambrian detrital monazite and zircon from the Hida gneiss on Oki-Dogo Island, Japan: their origin and implications for the correlation of basement gneiss of Southwest Japan and Korea. *Tectonophysics* **235**, 277–92.

Suzuki K and Adachi M (1998) Denudation history of the high T/P Ryoke metamorphic belt, Southwest Japan; constraints from CHIME monazite ages of gneisses and granitoids. *Journal of Metamorphic Geology* **16**, 23–37.

Suzuki K and Kato T (2008) CHIME dating of monazite, xenotime, zircon and polycrase: protocol, pitfalls and chemical criterion of possibly discordant age data. *Gondwana Research* **14**, 569–86.

Taylor RJM, Clark C, Fitzsimons ICW, Santosh M, Hand M, Evans N and McDonald B (2014) Post-peak, fluid-mediated modification of granulite facies zircon and monazite in the Trivandrum Block, southern India. *Contributions to Mineralogy and Petrology* **168**, 1–17.

Taylor RJM, Kirkland C and Clark C (2016) Accessories after the facts: constraining the timing, duration and conditions of high-temperature metamorphic processes. *Lithos* **264**, 239–57.

Tickyj H, Hartmann LA, Vasconcellos MAZ, Philipp RP and Remus MVD (2004) Electron microprobe dating of monazite substantiates ages of major geological events in the southern Brazilian shield. *Journal of South American Earth Sciences* **16**, 699–713.

White RW, Powell R and Holland TJB (2001) Calculation of partial melting equilibria in the system $Na_2O\text{-}CaO\text{-}K_2O\text{-}FeO\text{-}MgO\text{-}Al_2O_3\text{-}SiO_2\text{-}H_2O$ (NCKFMASH). *Journal of Metamorphic Geology* **19**, 139–53.

White RW, Powell R and Holland TJB (2007) Progress relating to calculation of partial melting equilibria for metapelites. *Journal of Metamorphic Geology* **25**, 511–27.

Whitney DL and Evans BW (2010) Abbreviations for names of rock-forming minerals. *American Mineralogist* **95**, 185–7.

Williams ML, Jercinovic MJ, Goncalves P and Mahan K (2006) Format and philosophy for collecting, compiling and reporting microprobe monazite ages. *Chemical Geology* **22**, 1–15.

Williams ML, Jercinovic MJ and Hetherington CJ (2007) Microprobe monazite geochronology: understanding geologic processes by integrating composition and chronology. *Annual Review of Earth and Planetary Sciences* **35**, 137–75.

Williams ML, Jercinovic MJ and Terry MP (1999) Age mapping and dating of monazite on the electron microprobe: deconvoluting multistage tectonic histories. *Geology* **27**, 1023–6.

Yedekar DB, Jain SC, Nair KKK and Dutta KK (1990) The Central Indian collision suture. Precambrian of Central India. *Geological Survey of India, Special Publication* **28**, 1–37.

Yin A, Dubey CS, Webb AAG, Kelty TK, Grove M, Gehrels GE and Burgess WP (2010) Geologic correlation of the Himalayan orogen and Indian Craton: Part I. Structural geology, U–Pb zircon geochronology, and tectonic evolution of the Shillong Plateau and its neighbouring regions in Northeast India. *Geological Society of America Bulletin* **122**, 336–59.

Zhu XK and O'Nions RK (1999) Monazite chemical composition: some implications for monazite geochronology. *Contributions to Mineralogy and Petrology* **137**, 351–63.

Zhu XK, O'Nions RK, Belshaw NS and Gibb AJ (1997) Lewisian crustal history from in situ SIMS mineral chronometry and related metamorphic textures. *Chemical Geology* **136**, 205–18.